Manuscript title:

Mapping protein distribution in the canine photoreceptor sensory cilium and calyceal processes by ultrastructure expansion microscopy

Authors and affiliations:

Kei Takahashi[1], Raghavi Sudharsan[1], William A. Beltran[1] *

[1]Division of Experimental Retinal Therapies, Department of Clinical Sciences & Advanced Medicine, School of Veterinary Medicine, University of Pennsylvania, Philadelphia, PA 19104

***Correspondence**: William A. Beltran, Division of Experimental Retinal Therapies, Department of Clinical Sciences & Advanced Medicine, School of Veterinary Medicine, University of Pennsylvania, 3900 Delancey Street, Philadelphia, PA, 19104, USA. Email: wbeltran@vet.upenn.edu

Keywords

Canine retina, Connecting cilium, Calyceal processes, Photoreceptor sensory cilium, Ultrastructure expansion microscopy

Abstract

Photoreceptors are highly polarized sensory neurons, possessing a unique ciliary structure known as the photoreceptor sensory cilium (PSC). Vertebrates have two subtypes of photoreceptors: rods, which are responsible for night vision, and cones, which support daylight vision and color perception. Despite identifying functional and morphological differences between these subtypes, ultrastructural analyses of the PSC molecular architecture in rods and cones are still lacking. In this study, we employed ultrastructure expansion microscopy (U-ExM) to characterize the molecular architecture of the PSC in canine retina. We demonstrated that U-ExM is applicable to both fresh and cryopreserved retinal tissues with standard paraformaldehyde fixation. Using this validated U-ExM protocol, we revealed the molecular localization of numerous ciliopathy-related proteins in canine photoreceptors. Furthermore, we identified significant architectural differences in the PSC, ciliary rootlet, and calyceal processes between canine rods and cones. These findings pave the way for a better understanding of alterations in the molecular architecture of the PSC in canine models of retinal ciliopathies.

Introduction

Photoreceptors are highly polarized sensory neurons, located in the outermost layer of the neuroretina that play a crucial role in light detection and signal transduction. In vertebrate retinas, there are two subtypes of photoreceptors: rods, which are highly sensitive to light and essential for night vision, and cones, which provide high visual acuity, color perception, and daylight vision [1]. These cells possess a unique sensory ciliary structure known as the photoreceptor sensory cilium (PSC). Within the PSC, photoreception and phototransduction occur in the outer segment (OS), a highly elaborated membrane structure supported by a nine-fold microtubule axoneme that originates from the basal body (BB) in the inner segment (IS). The region connecting the OS and IS, termed the connecting cilium (CC), is characterized by Y-shaped linkers (Y-links) that anchor each microtubule axoneme to the cell membrane and function as a critical gateway for ciliary trafficking [2, 3] (**Figure 1**). These fundamental features of the tubulin-based PSC architecture are thought to be shared between rods and cones, although detailed structural analyses for cone PSC are still lacking [4].

Using cryo-electron tomography, the ultrastructure of rod PSC has been thoroughly analyzed in the mouse retina, revealing that the CC structure of mouse rods is approximately 1.1 μm in length and 300 nm in diameter [5]. Additionally, immunogold electron microscopy has been employed to investigate the precise localization of proteins within this small subcellular compartment, identifying the distribution of several ciliary proteins in mouse rod PSC [6-8]. However, despite the identification of pathogenic variants in over 50 genes associated with non-syndromic retinal ciliopathies [9], the specific roles and precise distribution of these proteins within the PSC have remained largely uncharacterized due to the limited resolution and detection capabilities of conventional fluorescence immunohistochemistry.

With recent advances in super-resolution imaging techniques, it has become feasible to analyze detailed protein localization and morphology within the PSC using fluorescence immunostaining [10-13]. Notably, expansion microscopy (ExM), a sample preparation-based approach in which the specimen is expanded with a swellable hydrogel polymer and allows for ultrastructure observation without the need for specialized microscopy equipment, has become widely accessible to researchers [14]. Numerous

59 modified ExM protocols have been developed to optimize imaging for specific subcellular compartments
60 and sample conditions [15], some of which have been successfully applied to investigate the
61 ultrastructure of photoreceptors [16-18]. Among these advanced methods, ultrastructure expansion
62 microscopy (U-ExM) is particularly notable for its ability to preserve the native intracellular architecture of
63 biological specimens while enabling nanometer-scale observation using standard primary and secondary
64 antibodies used in immunohistochemistry [19]. U-ExM has already made significant contributions to the
65 molecular mapping of the mouse PSC and the detailed assessment of AAV-based gene augmentation
66 therapy in mouse retinal ciliopathy models [18, 20, 21].

67 Mice are frequently employed in research on PSC morphology and inherited retinal diseases (IRDs),
68 including retinal ciliopathies, due to their ease of handling, low breeding costs, and suitability for gene
69 editing. However, there are significant functional and structural differences between rodent and human
70 photoreceptors, such as very low percentage of cones, the absence of a foveomacular region, and the
71 lack of calyceal processes [22-24]. To address these limitations and enhance the relevance of preclinical
72 animal models, large animals such as dogs, cats, and pigs are proving to be valuable IRDs models.
73 Notably, canine models hold promise for advancing our understanding of the pathogenic mechanisms of
74 IRDs, owing to their fovea-like cone-rich structure [25] and the identification of an increasing number of
75 naturally-occurring genetic mutations linked to human IRDs [26]. Despite this potential, detailed
76 morphological studies on canine photoreceptors remain limited. In this study, we utilize U-ExM to
77 characterize the molecular architecture of the normal adult canine PSC. We validate the U-ExM method
78 for long-term cryopreserved canine retinal samples and provide a comprehensive analysis of the
79 architectural features of the canine PSC. This includes differences in PSC structure between rods and
80 cones, the distribution of retinal ciliopathy-related proteins, and the presence or absence of calyceal
81 processes.

Results

U-ExM protocol is effective on fresh and cryopreserved canine retinal tissues

To investigate whether U-ExM could be applied to canine retinal tissues, we tested a U-ExM protocol recently adapted for mouse retina [18] on adult canine retinal tissues subjected to different fixation and storage conditions. The short fixation condition (4% paraformaldehyde (PFA) for 15 minutes) is the same as that used for mouse retina in the previous U-ExM study, while a longer fixation protocol (4% PFA for 3 hours followed by 2% PFA for 24 hours) is routinely used by our lab for long-term cryopreservation of canine retinal tissues.

First, we assessed the structural preservation of the photoreceptor OS after expansion under each sample condition. In fresh retinas fixed for the short duration, the OS were severely damaged and unevenly swollen (**Figure 2A**). In contrast, the OS structures of both rods and cones were better preserved in the retinas fixed for the longer duration (**Figure 2B**). Similarly, the OS of the cryosection-derived U-ExM samples exhibited relatively better preservation compared to the short-fixed fresh retina, although they showed mild damage (**Figure 2C**). Since slight damage to the OS structure was observed even in the unexpanded cryosections (**Figure 2D**), it is likely that the quality of the cryosectioning was reflected in the sample after expansion.

Next, to verify whether the expansion factor was affected by fixation duration and storage conditions in canine retinal tissues, we compared the structure of the tubulin axoneme of the PSC under each sample condition. Although non-acetylated tubulin has frequently been used as a PSC axoneme marker in previous U-ExM studies using mouse retina [18, 20, 21], this labeling also showed a distinct signal in the photoreceptor IS. In contrast, immunostaining with antibodies targeting acetylated α-tubulin (AcTub), a widely used marker of primary cilia, labeled the PSC axoneme with high specificity (**Figure 2E**). Furthermore, labeling of acetylated and non-acetylated tubulin at the BB and CC of the PSC showed identical localization in the magnified images of the U-ExM samples (**Figure 2F-H**). Therefore, we employed AcTub as a highly specific marker for the PSC axoneme in subsequent studies. The width of the AcTub-labeled axoneme on the CC and the proximal end of the mother centriole (MC) after

108 processing by U-ExM was comparable across all sample conditions (**Figure 2J and K**). By dividing the
109 CC axoneme width of U-ExM samples by 200.84 nm, which is the previously reported CC axoneme width
110 of mouse photoreceptors [5], we determined an average expansion factor of 3.83 across all sample
111 conditions. Similarly, the gel diameter immediately after the first-round of expansion reached
112 approximately 5 cm in all sample conditions (**Supplementary Figure 2I**), averaging a 4.17 times larger
113 dimension than the original gel diameter. These values are not significantly different from the typical
114 expansion factor (~4) reported in previous U-ExM studies [18, 19].

115 We further investigated the localization patterns of representative CC-associated proteins to verify
116 whether there are differences in the localization of these proteins among the different sample conditions.
117 Centrin and CEP290 (NPHP6), which have been well characterized in mouse photoreceptors as the CC
118 inner scaffold protein and Y-link-associated protein, respectively [18], were examined. In U-ExM
119 processed canine photoreceptors, Centrin localized specifically inside the tubulin axoneme of the BB and
120 CC (**Figure 2L-N**), while CEP290 was observed outside the CC axoneme (**Figure 2P-R**), consistent with
121 their previously reported localization patterns. Moreover, there were no significant differences in the
122 localization of these proteins among the different sample conditions. In summary, our findings confirmed
123 that U-ExM could be utilized for canine retinal tissue and that variations in PFA fixation and storage
124 conditions do not affect the expansion factor. Considering the better preservation of OS structure, we
125 used long-fixed fresh retinas and frozen archival retinal tissues for the subsequent studies described
126 below.

127

128 **Differences in tubulin-based molecular architecture between rod and cone PSC**

129 We then analyzed the molecular architecture of the tubulin axoneme in rod and cone PSC of normal
130 adult canine retinas processed by U-ExM. Rod and cone photoreceptors were distinguished by labeling
131 with rhodopsin and cone arrestin (CAR), respectively. The tubulin axoneme in both photoreceptor
132 subtypes was visualized by labeling acetylation and glutamylation on the tubulin, which are well-known
133 post translational modifications in the centriole and primary cilium, using AcTub and GT335 antibodies.

134 In both photoreceptor subtypes, glutamylation was detected on the tubulin axoneme throughout the PSC,
135 similar to acetylation. The glutamylation signal was also found outside the tubulin axoneme only around
136 the CC region (**Figure 3A-D**). A recent study suggested that glutamylation signal shows localization
137 comparable to CEP290 in mouse photoreceptor CC [18]. Similarly, we identified that the region of the
138 glutamylation signal on the tubulin axoneme matches the CEP290 signal on the CC in canine
139 photoreceptors (**Supplementary Figure 3**). Based on these findings, we assumed that the region with
140 glutamylation outside the tubulin axoneme is equivalent to the CC and measured the length and width of
141 each compartment of the PSC axoneme (**Figure 3E**). As previously reported for other cell types [27, 28],
142 the length of the MC was significantly longer than that of the daughter centriole (DC) in each
143 photoreceptor subtype. More interestingly, cone photoreceptors had notably longer BBs than rods (Rod
144 DC, 269.71 ± 24.00 μm; Cone DC, 357.27 ± 37.26 μm; Rod MC, 372.06 ± 55.22 μm; Cone MC, 465.84
145 ± 40.58 μm; **Figure 3F**). In contrast, the length of the CC in cones was significantly shorter than that in
146 rods (Rod CC, 1362.81 ± 164.22 μm; Cone CC, 900.35 ± 169.02 μm; **Figure 3H**). The width of the AcTub-
147 labeled tubulin axoneme in the CC and BBs was identical among the photoreceptor subtypes (**Figure 3G**
148 **and I**).

149 Next, we focused on the differences between rod and cone tubulin structures in the outer region of
150 the CC, referred to as the bulge region (BR). Based on the measurement method used in previous studies
151 on mouse photoreceptors [18, 21], we measured the width of the tubulin axoneme at multiple positions
152 along the CC in rod and cone photoreceptors: at the distal end of the CC (0), as well as 500 and 1000
153 nm above (+500, +1000) and 500 nm below (-500) (**Figure 3J and K**). In the rod PSC, the width of the
154 tubulin axoneme significantly increased from the end of the CC to the +500 nm, then decreased to the
155 +1000 nm (**Figure 3L**). Conversely, in the cone PSC, the enhanced width of tubulin axoneme from the
156 CC endpoint to the +500 nm was maintained even at the +1000 nm (**Figure 3M**). When comparing the
157 axoneme width between rods and cones at each measurement point, the cone axoneme was significantly
158 wider than the rod axoneme at all points except the middle part of the CC (-500) (**Figure 3N**). These
159 results revealed that cone photoreceptors have longer and wider BR than rod photoreceptors.

160

161 **Molecular mapping of the bulge region and distal axoneme in canine rod and cone PSC**

162 To further characterize the differences in molecular architecture at the distal part of the tubulin
163 axoneme between rods and cones in detail, we investigated the location of several proteins associated
164 with the BR and distal axoneme in both rods and cones. LCA5 (lebercilin) has been identified as a BR-
165 specific protein in mouse photoreceptors [18, 21]. Consistent with the results from previous studies, LCA5
166 showed specific localization to the inner side of the BR in both rod and cone photoreceptors in the canine
167 PSC (**Figure 4A and B**). Additionally, RP1, known to localize from the BR to the distal axoneme in mouse
168 photoreceptors [21], exhibited a comparable localization pattern in canine rod and cone photoreceptors
169 (**Figure 4C and D**). In this study, we identified CCDC66 as a novel protein that specifically localizes to
170 the distal axoneme of both rods and cones (**Figure 4E and F**). CCDC66 is a microtubule-binding protein,
171 and dysfunction of its gene has been reported to cause retinal degeneration in both canine and mouse
172 models [29-31]. Consistent with previous findings where overexpressed CCDC66 in a cell line with
173 induced ciliogenesis was observed near the BB and distal axoneme [32], endogenous CCDC66 in canine
174 photoreceptors also showed a weak signal near the BB and a prominent signal at the distal axoneme.

175 To elucidate the positional relationship of these three proteins in the distal part of the PSC axoneme,
176 we performed co-immunostaining of RP1 with LCA5 and CCDC66, respectively. In both rods and cones,
177 LCA5 localized slightly more basally than RP1, and these two proteins did not co-localize (**Figure 4G**
178 **and H**). Additionally, axial view images showed that LCA5 localized on the tubulin axoneme while RP1
179 localized outside the axoneme (**Figure 4I**). CCDC66 appeared to overlap with RP1 in the distal axoneme
180 in the lateral view (**Figure 4J and K**). However, in the axial view, CCDC66 was localized inside the tubulin
181 axoneme, distinct from the localized area of RP1 (**Figure 4L**). By measuring the distance from the
182 proximal end of the MC to the starting point of each signal, we found that in cones, LCA5 and RP1
183 localized more basally compared to rods, while CCDC66 localized more distally (**Figure 4M**). Taken
184 together, LCA5, RP1, and CCDC66 each exhibited unique localization patterns in the distal part of the
185 PSC, and differences in localization of these proteins between rod and cone coincided with the

186 architectural differences in the BR between these photoreceptor subtypes (**Figure 4N**).

187

188 **Molecular mapping of the connecting cilium in canine rod and cone PSC**

189 Next, we compared the localization of CC-related proteins between rods and cones. POC5, Centrin,
190 and FAM161A have been well-characterized to localize inside the tubulin axoneme as inner scaffold
191 proteins at the BB and CC in mouse photoreceptors [18]. Consistent with the reports in mouse
192 photoreceptors, these three inner scaffold proteins exhibited internal localization within the axoneme at
193 the BB and CC in both canine photoreceptor subtypes (**Figure 5A-I**). Since the endogenous FAM161A
194 signal was too weak to quantify (**Figure 5G-I**), similar to results in mouse photoreceptors [18, 20], we
195 measured the signal length in the CC for only POC5 and Centrin (**Figure 5J**). The signal lengths of these
196 inner scaffold proteins at the CC were significantly shorter in cones than in rods, and these were
197 consistent with the CC lengths measured in Figure 3 (Rod POC5, 1383.09 ± 96.53 μm; Cone POC5,
198 911.01 ± 129.72 μm; Rod Centrin, 1449.83 ± 115.57 μm; Cone Centrin, 989.27 ± 172.09 μm; **Figure 5K**).

199 We then investigated the localization of several Y-link-associated proteins in canine photoreceptors.
200 The Y-link is a hallmark element of the transition zone in the primary cilium, exhibiting a distinctive Y-
201 shaped architecture that connects each microtubule doublets to the ciliary membrane [3]. In mammalian
202 photoreceptors, the CC is known as a region corresponding to the transition zone in the primary cilium,
203 and CEP290, a typical Y-link component protein, has been confirmed to localize outside each of the nine
204 tubulin axonemes in the CC of mouse photoreceptors [18]. As shown in Figure 2 and Supplementary
205 Figure 3, CEP290 localized at the CC in canine photoreceptors similar to its localization in mouse
206 photoreceptors. Here, we also found that the signal length of CEP290 at the CC is significantly shorter in
207 cones than in rods, consistent with the lengths of the CC shown in Figure 3 and Figure 5 (Rod CEP290,
208 1314.33 ± 118.71 μm; Cone CEP290, 891.09 ± 126.21 μm; **Figure 6A, B, C, and S**). Additionally, several
209 other Y-link-associated proteins, including RPGR, RPGRIP1 (LCA6), SPATA7 (LCA3), and NPHP5
210 (IQCB1), were found to have signal lengths comparable to CEP290 at the CC in both rods and cones
211 (**Figure 6D, E, G, H, J, K, M, N, and S**) and to localize outside the axoneme (**Figure 6F, I, L, O, and R**).

212 Finally, we found that MAP9, a microtubule-binding protein, localizes specifically to the CC in
213 photoreceptors (**Figure 6P and Q**). A homozygous variant in the MAP9 gene has been reported to
214 accelerate disease progression in a naturally-occurring canine *RPGRIP1*-associated cone-rod dystrophy
215 [33, 34]. The co-localization of MAP9 and RPGRIP1 in the CC of both photoreceptor subtypes suggests
216 a direct interaction between these proteins. Additionally, axial view images and quantification of signal
217 width at the CC revealed that MAP9 is located close to the tubulin axoneme, unlike the axial distribution
218 of other Y-link-associated proteins (**Figure 6R and T**). Mapping of these CC-specific proteins confirmed
219 a significant difference in the length of the CC between canine rods and cones.
220

221 **Molecular mapping of ciliary trafficking and distal appendage-related proteins on the basal bodies**
222 **in rod and cone PSC**

223 We next mapped the localization of proteins associated with the BBs, the compartment on the basal
224 part of the tubulin-based PSC architecture. The intraflagellar transport (IFT) machinery is responsible for
225 anterograde and retrograde trafficking of ciliary proteins and consists of two multisubunit complexes, IFT-
226 A and IFT-B [35]. In mouse photoreceptors, it was demonstrated using immunoelectron microscopy that
227 several IFT particles have characteristic distribution around the MC and BR [8], and similar localization
228 of these particles has recently been confirmed using U-ExM as well [20, 21]. We confirmed that in both
229 canine rods and cones, IFT57, a component of the IFT-B complex [36], has a similar distribution at the
230 MC and BR as observed in mouse photoreceptors (**Figure 7A and B**). Additionally, KIF3A, a component
231 of kinesin-II, exhibited a similar distribution to the IFT particles in both photoreceptor subtypes, albeit with
232 a high level of background signal (**Supplementary Figure 4**). Axial view images showed that IFT57
233 distributes along each of the nine tubulin axonemes at both the MC and BR and is located closer to the
234 axonemes at the BR than at the MC (**Figure 7C**). We also found that the IFT57 signals at the MC were
235 clearly divided into two layers (**Figure 7A and B**). The distance from the proximal end of the MC to these
236 signals was shorter in rods than in cones (**Figure 7D**), consistent with the difference in BB length between
237 the rods and cones presented in Figure 3.

238 Based on the characteristic distribution of IFT57 in the MC, we hypothesized that the IFT molecules
239 localize around distal appendages, also known as transition fibers, in the MC, as has been suggested in
240 previous publications [37, 38]. To verify this, we observed the distribution of CEP164 (NPHP15), a
241 representative distal appendage protein [39], in both rods and cones. As expected, CEP164 was localized
242 in the distal part of the MC in both rods and cones (**Figure 7E and F**), and the axial view exhibited a
243 broader radial distribution (**Figure 7G**), similar to that observed in recent studies using super-resolution
244 microscopy techniques [40, 41]. The distance from the MC proximal end to CEP164 signals was shorter
245 in rods than in cones, and these distances were comparable to these of the IFT57 signals at the distal
246 MC (**Figure 7D and M**).
247 Additionally, we found that SDCCAG8 (NPHP10), a retinal ciliopathy-associated protein [42, 43],
248 exhibits specific localization to the end of both MC and DC in rods and cones (**Figure 7H and I**). The
249 axial view images at the MC showed that SDCCAG8 has a nine-fold symmetry distribution outside the
250 axoneme, similar to IFT57 and CEP164 (**Figure 7J**). Moreover, co-immunostaining of SDCCAG8 with
251 glutamylation and γ-tubulin demonstrated that the SDCCAG8 signal on the ciliary axoneme is located
252 between the MC and CC (**Figure 7K and L**). The distance from the MC proximal end to SDCCAG8 was
253 comparable to that of CEP164 in both rods and cones (**Figure 7M**). Taken together, these results suggest
254 that IFT57 and SDCCAG8 localize to distal appendages on the MC (**Figure 7N**). Furthermore, based on
255 the distance between distal and subdistal appendages suggested in previous study (~100 nm), the
256 location of the basal IFT57 signal in the MC is assumed to correspond to the location of the subdistal
257 appendages [44].
258
259 **Molecular architecture of the ciliary rootlet in canine photoreceptors**
260 To address the peripheral structures of the PSC in canine photoreceptors, we mapped several
261 proteins related to the ciliary rootlet. Rootletin (CROCC) is a 220-kDa coiled coil protein identified as an
262 architectural component of the rootlet in mouse photoreceptors [45] and has been used as a marker of
263 ciliary rootlet in several studies [46, 47]. Consistent with previous reports, in canine retinas processed

264 with U-ExM, rootletin signals were observed as straight fibers in the photoreceptor IS, representing the
265 architecture of the ciliary rootlets (**Figure 8A**). In the magnified images, a rootlet stem extending straight
266 to the MC and a characteristic branch-like structure extending to the middle of the CC were observed in
267 the rod PSC (**Figure 8B and C, Supplementary Movie 1**). In contrast, cone photoreceptors exhibited a
268 curvilinear rootlet architecture that was quite different from that of rods. In cone photoreceptors, the base
269 of the rootlet did not contact the external limiting membrane, unlike in rods, and the ends of the rootlet
270 appeared to be directed toward the MC and DC, respectively (**Figure 8D and E, Supplementary Movie**
271 **2**). These structural features in cones were consistent among cone photoreceptor subtypes, S-cones and
272 L/M-cones (**Supplementary Figure 5**).

273 We found that ARL13B, a small GTPase belonging to the Arf-like Ras superfamily, is another protein
274 located in the ciliary rootlet of canine photoreceptors. In studies of the primary cilium, ARL13B has
275 frequently been employed as a marker for the ciliary membrane [48, 49]. Since mutations in *ARL13B*
276 gene have been associated with Joubert syndrome, a systemic ciliopathy accompanied by retinal
277 dystrophy, the localization of ARL13B in photoreceptors has been discussed in various studies, with
278 variable conclusions [50-53]. Although several recent reports using mouse retina have claimed that
279 endogenous ARL13B localizes to the photoreceptor OS [54, 55], we found specific localization of ARL13B
280 to the ciliary rootlet in U-ExM-processed canine photoreceptors (**Figure 8F**). We performed similar
281 immunostaining on non-expanded cryosections to confirm that this ARL13B localization pattern, which
282 differs from recent reports, is not due to an artifact of the U-ExM process. In non-expanded canine retina,
283 ARL13B localized primarily to the photoreceptor IS, consistent with the results in the U-ExM samples
284 (**Supplementary Figure 6**). Similar to rootletin, ARL13B exhibited straight localization in rods and
285 curvilinear localization in cones (**Figure 8G and H**).

286

287 **Molecular architecture of the calyceal processes in canine photoreceptors**

288 Finally, we investigated the localization of protocadherin-15 (PCDH15), an Usher protein, to
289 determine the presence or absence of calyceal processes in canine photoreceptors. Calyceal processes

290 are microvilli-like structures characterized by the localization of Usher proteins in the apical region of the
291 IS of human and nonhuman primate (NHP) photoreceptors, and are absent in mouse photoreceptors [24].
292 Recent research on NHP photoreceptors using expansion microscopy has described the structural
293 organization of the calyceal processes based on the distribution of PCDH15 [17]. We followed this
294 approach on our canine retinal tissues. First, we determined that PCDH15 is located between the OS
295 and IS in both rods and cones in non-expanded retinal cryosections (**Figure 9A**). In the canine rod
296 photoreceptors processed by U-ExM, PCDH15 staining exhibited a characteristic C-shape, and its
297 distribution was limited to the base of the OS (**Figure 9B, Supplementary Movie 3**). In contrast, PCDH15
298 formed a microvilli-like structure surrounding the OS near the OS/IS junction in the canine cones (**Figure**
299 **9C, Supplementary Movie 4**). The distribution pattern of PCDH15 was identical between S-cones and
300 L/M-cones (**Figure 9D and E**). These differences of PCDH15 distribution between rods and cones were
301 consistent with the previous observations in NHP photoreceptors [17]. Additionally, we attempted to
302 localize another Usher protein, VLGR1 (USH2C), in canine photoreceptors. However, identification of
303 specific VLGR1 signals using a commercially available primary antibody was unsuccessful. Finally, we
304 located actin filaments by immunolabeling of β-actin. Unlike the previous observation in NHP rod
305 photoreceptors, no actin filaments binding to PCDH15 were observed in canine rods. However, canine
306 cones exhibited actin filaments linking to PCDH15-labeled calyceal processes (**Figure 9F**). Taken
307 together, these results suggest that in canine photoreceptors, although the distribution of PCDH15 at the
308 IS/OS junction is found in rods, the calyceal processes-like architecture is present only in cone
309 photoreceptors, similar to NHP photoreceptors (**Figure 9G**).

310 ## Discussion

311 In the present study, we tested a U-ExM protocol to characterize the molecular architecture of the
312 PSC using fresh and frozen archival canine retinal tissues. Utilizing archival samples, particularly from
313 large animals such as dogs and NHP, presents significant advantages in terms of cost efficiency and
314 biological resource management. This approach is not only economical but also allows for the
315 maximization of previously collected biological materials. However, as highlighted in the publication
316 reporting the original U-ExM protocol, the type and duration of fixation can influence the degree of tissue
317 expansion [19]. Earlier studies applying U-ExM to the mouse retina typically used a short duration (15
318 minutes) of 4%PFA fixation [18, 21]. Here, we demonstrated that the duration of PFA fixation and long-
319 term storage at -80°C do not significantly impact the degree of retinal tissue expansion, achieving
320 approximately 4x isotropic expansion (**Figure 2**). This observation aligns with the recent reports that
321 applied U-ExM to PFA-fixed frozen and formalin-fixed paraffin-embedded mouse tissues [20, 28]. Notably,
322 our results showed that U-ExM enabled super-resolution imaging of archival samples that had been
323 cryopreserved for over a decade, providing comparable imaging quality to that obtained from fresh
324 samples. Additionally, longer durations of PFA fixation (≥ 24 hours), which are routinely used for
325 cryopreservation of ocular tissues, proved beneficial in preserving the structure of the photoreceptor OS
326 in U-ExM. These findings underscore the robustness of U-ExM for use with archival samples, facilitating
327 ultrastructural observation in large animal tissues where fresh samples are often challenging to procure.

328 In the molecular mapping of the PSC in normal adult canine retinal tissue, we discovered that the
329 tubulin-based PSC architecture differs significantly between the rods and cones (**Figure 3**). Specifically,
330 cones exhibited longer BBs, which encompass both the DM and MC, as well as shorter CC, and longer,
331 wider BR compared to rods. These structural differences were corroborated by the distinct localization
332 patterns of proteins within each PSC compartment (**Figure 4-7**). While detailed comparisons of PSC
333 molecular architecture between rods and cones have been limited, our findings align with the known
334 variations in the structural features of the OS between these photoreceptor subtypes [56]. Previous
335 studies have consistently reported that the CC length in mature mouse rods ranges from approximately

336 1100 to 1500 nm [5, 18, 21], which is consistent with the CC-specific protein signal lengths of
337 approximately 1200 to 1400 nm observed in mature canine rods in this study. Similarly, the DC length in
338 mature mouse rods is approximately 300 nm [5], closely matching the 270 nm measured in mature canine
339 rods, indicating a conserved architecture of the CC and BB in rods across these species. However,
340 comparisons of cone PSC architecture between canine and other vertebrates remain challenging due to
341 a paucity of studies investigating the ultrastructure of cone PSC to date. The significant architectural
342 differences between rod and cone PSC observed in this study underscore the necessity for further
343 comprehensive investigations using retinal tissues from a variety of vertebrate species. These
344 investigations are crucial to determine whether the architectural distinctions in the PSC between
345 photoreceptor subtypes are unique to canine or represent a broader biological phenomenon.

346 An interesting question raised by the observed architectural variation between rod and cone PSC is
347 its involvement in the differential pathological progression among photoreceptor subtypes. A notable
348 group of retinal ciliopathies, known as cone-rod dystrophy (CRD), is characterized by the progressive
349 degeneration of cones preceding that of the rods. In canine models of naturally-occurring retinal ciliopathy,
350 homozygous variants in genes such as *NPHP4*, *NPHP5*, and *RPGRIP1* have been identified as causes
351 of CRD [57-59], despite these genes being similarly expressed in both rods and cones. Previous studies
352 have suggested that these CRD-associated proteins are localized to the CC in photoreceptors [11, 60].
353 Our current study confirms that NPHP5 and RPGRIP1 are indeed localized outside the tubulin axoneme
354 at the CC in both photoreceptor subtypes (**Figure 6**). Given their comparable distribution, these proteins
355 are likely to have similar roles related to Y-links in both photoreceptor subtypes. Notably, the CC, where
356 the tubulin axoneme of the PSC is anchored to the plasma membrane by Y-links, is significantly shorter
357 in cones than in rods. This structural difference in the CC suggests that cones may be more susceptible
358 to mutations in Y-link-associated genes compared to rods. The relationship between the heterogeneity of
359 ciliopathy-associated phenotypes and the structural variations between rods and cones will be further
360 investigated in future studies, which will involve integrating respective retinal ciliopathy models with U-
361 ExM techniques to elucidate these differences.

362 Our study has also revealed significant difference in the architecture of the PSC rootlet between rods
363 and cones (**Figure 8**). Using U-ExM, we observed a linear shape of the rootlet in canine rods, which is
364 consistent with the morphology of the rootlet in mouse rods, as previously described in transmission
365 electron photomicrographs [10]. A new finding in this study is the identification of a rootlet branch
366 extending from the basal part of the PSC to the middle of the CC in rods. This branching structure has
367 also been observed in recent transmission electron photomicrographs of canine photoreceptors, where
368 it appears to be positioned on the opposite side of the PSC axoneme across the ciliary pocket [61],
369 although its functional role remains unclear. Another interesting discovery is the unique elliptical shape
370 of the cone rootlet. A recent study in NHP cones suggests that the cone rootlet has a markedly different
371 shape from the commonly recognized form in rod rootlet, although detailed morphological descriptions
372 have been lacking [17]. Here, we have demonstrated a curvilinear rootlet architecture in canine cones
373 using U-ExM. Additionally, unlike the rod rootlet, which extends towards the external limiting membrane,
374 the cone rootlet is entirely contained within the photoreceptor IS. Both rootlet structures likely play a
375 critical role in providing stable intracellular support for the PSC and their associated OS structures.
376 However, further studies are needed to elucidate the biological significance of these morphological
377 differences between rod and cone photoreceptors.

378 Finally, the application of U-ExM provided novel insights into the architecture of calyceal processes
379 in canine photoreceptors (**Figure 9**). Our findings indicate that canine cones possess microvilli-like
380 structures characterized by the distribution of PCDH15 around the basal part of the OS and the presence
381 of associated actin filaments. In contrast, canine rods lack calyceal processes-like structures, despite the
382 localization of PCDH15 at the IS/OS junction. These structural differences between rods and cones are
383 similar to those observed in photoreceptors of NHPs in a previous study [17]. To conclusively determine
384 the presence or absence of calyceal processes in canine rods, further detailed morphological studies
385 using electron microscopy are necessary. However, the localization of PCDH15 in canine photoreceptors
386 aligns with the patterns reported in NHP photoreceptors, suggesting that a canine IRD model may provide
387 valuable insights into pathogenesis of Usher syndrome, for which effective pathological models are

388 challenging to develop in rodents.

389 In conclusion, our study highlights the effectiveness of super-resolution imaging using U-ExM to
390 characterize the molecular architecture of the canine PSC. By employing U-ExM, we have achieved
391 detailed molecular mapping of numerous retinal ciliopathy-related proteins and have identified significant
392 structural differences in the PSC between rods and cones in canine photoreceptors (**Figure 10**). These
393 insights gained from this study pave the way for a better understanding of the alterations in PSC
394 molecular architecture and the efficacy of AAV-based gene augmentation therapies in established canine
395 models of retinal ciliopathy, such as those with mutations in *RPGR* [62], *NPHP5* [58], *RPGRIP1* [59], and
396 *CCDC66* [31], using U-ExM.

397

398 ## Material and methods

399 ### Animals

400 Retinal tissues from normal adult dogs were used for this study (**Supplementary Table 1**). All dogs
401 were housed under identical conditions, including diet and ambient illumination with a 12-hour light/12-
402 hour dark cycle, at the Retinal Disease Studies Facility (RDSF) at the University of Pennsylvania. The
403 studies strictly adhered to the ARVO Statement for the Use of Animals in Ophthalmic and Vision Research
404 and were approved by the Institutional Animal Care and Use Committee of the University of Pennsylvania.

405

406 ### Tissue processing for long-term cryopreservation

407 The procedures for long-term cryopreservation of normal adult canine ocular tissues were performed
408 as described in previous publications [63, 64]. In brief, following enucleation of euthanized dogs, the
409 posterior eyecups of the globes were isolated and the vitreous was gently extracted ~ 1 hour after fixation
410 in 4% PFA in 0.1 M phosphate-buffered saline (PBS). Fixation of the posterior eye cups was pursued for
411 an additional 2 hours, followed by an additional 24-hour fixation in 2% PFA in 0.1 M PBS at 4°C.
412 Subsequently, the eyecups were dissected into four quadrants, and the tissues were sequentially
413 cryoprotected for 24 hours each in 15% and 30% sucrose solutions in 0.1 M PBS at 4°C. Following
414 cryopreservation, the dissected tissues were embedded in optimal cutting temperature (OCT) medium
415 within disposable molds. The molds were then placed in shallow metal cups containing methylbutane
416 and immersed in a bath of liquid nitrogen for rapid freezing. The frozen OCT blocks were stored at -80°C
417 until cryosectioning was conducted. All cryopreserved samples used in this study had been stored for
418 more than 12 years at -80°C (**Supplementary Table 1**).

419

420 ### Immunohistochemistry on non-expanded cryosectioned retinal tissues

421 The frozen OCT blocks were cryosectioned at a thickness 10 μm and stored at -20°C until further
422 processing. Detailed methodology for immunostaining of non-expanded canine retinal cryosection has
423 been described in a previous publication [34]. Frozen sections were dried at room temperature (RT) for

424 60 minutes and then incubated in D-PBS for 10 minutes to remove the OCT compound. Antigen retrieval
425 was performed by treating the sections with pepsin reagent for 1 minute, followed by incubation with
426 blocking buffer (4.5% cold fish gelatin, 0.1% sodium azide, 5% bovine serum albumin, and 0.25% Triton
427 X-100 in D-PBS) for 60 minutes at RT. Retinal sections were then incubated overnight at 4°C with primary
428 antibodies (**Supplementary Table 3**) diluted in blocking buffer. After three washes with D-PBS containing
429 0.1% of tween20 (PBS-T), antigen-antibody complexes were visualized with Alexa Fluor-conjugated
430 secondary antibodies (**Supplementary Table 4**) and counterstained using Hoechst 33342. The reagents
431 used for conventional immunostaining were listed in Supplementary Table 2.
432
433 **Ultrastructure Expansion Microscopy (U-ExM) on canine retina**
434 Based on a U-ExM protocol previously developed for mouse retina [18], we tested U-ExM on fresh
435 and frozen archival canine retinal tissues. A schematic overview, photographs of each step, and reagents
436 associated with the U-ExM protocol used in this study are summarized in Supplementary Figure 1 and 2
437 and in Supplementary Table 2.
438 <u>(a) U-ExM on fresh canine neuroretinas</u>
439 After enucleation, the anterior part of eyeball, including the cornea, lens, and vitreous, was gently
440 removed. The posterior eyecups were fixed in PFA solution for either short (4% PFA for 15 minutes) or
441 long (4% PFA for 3 hours followed by 2% PFA for 24 hours) durations, and then 5 mm punches were
442 taken from the eyecups using a disposable biopsy punch (**Supplementary Figure 2A**). Once isolated
443 from RPE-choroid-sclera complex (**Supplementary Figure 2B, 2C**), a 5 mm retinal punch was placed in
444 a 14-mm microwell of a 35-mm petri dish and then incubated overnight in 300 μL of 2% acrylamide (AA)
445 + 1.4% formaldehyde (FA) solution at 37°C.
446 After removing the AA/FA solution, 45 μL of monomer solution (MS) composed of 25 μL of sodium
447 acrylate (SA; stock solution at 38% [w/w] diluted with nuclease-free water), 12.5 μL of AA (40% solution),
448 2.5 μL of N,N′-methylenebisacrylamide (BIS; 2% solution), and 5 μL of 10× PBS was added to the
449 microwell. After 90 minutes of incubation at RT, the MS was removed and 90 μL of MS containing

450 ammonium persulfate (APS) and tetramethylethylenediamine (TEMED) at a final concentration of 0.5%
451 was dropped onto the tissue, followed by covering with a 12 mm circular cover glass (**Supplementary**
452 **Figure 2D**). Subsequently, the 35-mm petri dish containing the tissue and MS solution was placed on ice
453 for 45 minutes, followed by 60 minutes incubation at 37°C to allow gelation.

454 Next, 1 mL of denaturation buffer (200 mM Sodium Dodecyl Sulfate (SDS), 200 mM Sodium Chloride
455 (NaCl), 50 mM Tris Base in deionized distilled water (ddH_2O), pH 9) were added to the petri dish for 15
456 minutes at RT with gentle agitation. The gel was carefully detached from the microwell using a spatula
457 and then incubated in a 1.5 mL tube filled with denaturation buffer for 90 minutes at 95°C. Immediately
458 after the denaturation step, the gel was transferred to a beaker filled with ddH_2O, and the ddH_2O was
459 replaced twice, every 30 minutes, for the first-round of expansion.

460 The following day, after measuring the diameter with a ruler (**Supplementary Figure 2E**), the
461 expanded gel containing retinal tissue was sliced with a razor blade to obtain approximately 1-2 mm thick
462 cross sections. These sections were then placed in a well of 24-well plate filled with D-PBS containing
463 calcium & magnesium (D-PBS-$Ca^{2+}Mg^{2+}$) for the immunostaining steps.

464 <u>(b) U-ExM for cryosections from frozen retinal tissue</u>

465 Twenty-μm-thick cryosections were obtained from the frozen posterior cup tissues that had been
466 fixed with PFA using the longer protocol, cryoprotected in sucrose, and embedded in OCT media. The
467 frozen sections on a slide glass were thawed at RT for 10 minutes (**Supplementary Figure 2F**), and a
468 square was drawn around the tissue section using a hydrophobic marker (ImmEdge Pen). After drying
469 for 60 minutes at RT, 100 μL of D-PBS-$Ca^{2+}Mg^{2+}$ was added into the hydrophobic square for 10 minutes
470 to wash out the OCT compound.

471 After removal of D-PBS, the sections were reacted with the AA/FA solution overnight, followed by
472 penetration with MS for 90 minutes, as was done for fresh retinal punches. For each retinal section, 45
473 μL of MS containing APS and TEMED per section was dropped onto the tissue, and a 12 mm circular
474 cover glass was placed on the solution (**Supplementary Figure 2G**). After performing gelation,
475 denaturation, and the first-round expansion as done for fresh retinal punches, the diameter of the gel was

476 measured with a ruler (**Supplementary Figure 2H**). The gel containing the retinal tissue was then cut
477 into approximately 1 cm squares using a razor blade and then in a well of 24-well plate filled with D-PBS-
478 $Ca^{2+}Mg^{2+}$.

479 Immunohistochemistry for U-ExM samples

480 After 10 minutes of incubation of the gels in D-PBS, the solution in the well was replaced with 300
481 µL of blocking buffer containing the primary antibodies (**Supplementary Table 3**). The gels were
482 incubated with the primary antibody solution overnight at RT with gentle shaking, followed by 3 washes
483 with 1 mL of PBS-T for 5 minutes each. Alexa Fluor-conjugated secondary antibodies (**Supplementary**
484 **Table 4**) were diluted in the blocking buffer at a concentration of 1/500 and incubated with the gel for 2
485 hours at RT, protected from light. Next, 100 µL of Hoechst 33342 solution, diluted 1/1000 in D-PBS, was
486 added to the wells and gently shaken for 30 minutes, followed by 3 washes with 1 mL of PBS-T. After the
487 washes, each gel was transferred using a spatula to a well of a 6-well plate filled with 10 mL ddH_2O and
488 incubated for 30 minutes to achieve the second-round expansion. The ddH_2O was replaced twice, every
489 30 minutes. The gels were then stored in ddH_2O at 4°C, protected from light, until confocal imaging.

490

491 **Confocal imaging**

492 Prior to imaging, 14-mm microwells of 35-mm petri dishes were filled with 0.1 mg/mL poly-D-lysine
493 and kept at RT for 1 hour for coating to prevent drifting of the gels. After removing the poly-D-lysine
494 solution, the microwells were washed three times with ddH_2O, dried, and then stored at 4°C.

495 Image acquisition was performed on the Leica Stellaris 8 FALCON confocal FLIM microscope using
496 a 63× (1.20 NA) water objective. The lateral and axial views were obtained by orienting the expanded gel
497 on the bottom of the microwell to face either the retinal cross-section or photoreceptor outer segment
498 downward. Z-stacks for the lateral view were acquired with 0.2 µm z-intervals, an x, y pixel size of 45.09
499 nm, and an imaging speed of 400 Hz. Representative images of the lateral view are shown as maximum
500 projection images unless specified. Sigle images of the axial view were obtained with an x, y pixel size
501 of 22.55 nm and an imaging speed of 100 Hz. The images were processed using Leica Application Suite

502 X (LAS X) software for deconvolution with LIGHTNING function, as well as for building merged and
503 maximum projection images, and 3D rendering.
504
505 **Quantification**
506 Gel diameter
507 The gel diameter after the first-round expansion was measured using a ruler and then divided by the
508 gel diameter before expansion (1.2 mm) to calculate the degree of gel expansion.
509 Expansion factor
510 The expansion factor was calculated by dividing the width of the AcTub-labeled axoneme on the CC
511 of U-ExM samples by the previously reported CC diameter of non-expanded mice photoreceptors (200.84
512 nm), quantified using cryo-electron tomography [5]. A total of 40 photoreceptors in all U-ExM conditions
513 were subjected to measurement of AcTub signal width using LAS X software manually. The width of the
514 CC was consistent across all U-ExM conditions, and the expansion factor in this study was determined
515 to be 3.83 by averaging the values of all U-ExM conditions. This expansion factor was used for every
516 quantification.
517 Protein signal length, width, and distance from the proximal end of the MC
518 Lengths, widths, and distance of protein signals were measured using the “Draw scalebar” function
519 in LAS X software manually to fit the photoreceptor curvature. AcTub-labeled axoneme spread was
520 measured at four different locations of the rod and cone photoreceptors corresponding to the CC or BR:
521 +1000, +500, 0, and -500 nm. The distal end of the glutamylation signal located outside the tubulin
522 axoneme was used to define the 0 location. Each measurement was subsequently corrected using the
523 expansion factor.
524
525 **Statistical analysis**
526 Comparisons between 2 groups were performed using the nonparametric Mann-Whitney U test.
527 Comparisons among more than 3 groups were conducted using the nonparametric Kruskal-Wallis test

with Dunn's multiple-comparison test. Every measurement was performed on at least 2 individual eyes. Quantitative data are represented as scatter dot plots, with the center line and error bars in the graphs indicating the mean and standard deviation (± SD), respectively. The significance level is denoted as follows: nonsignificant (n.s.) $P > 0.05$, *$P < 0.05$, **$P < 0.01$, ***$P < 0.001$, ****$P < 0.0001$. All statistical analyses were performed using GraphPad Prism 10. The data underlying the graphs shown in all the figures are included in Supplementary Data.

Data availability

All data are available in the main text or the supplementary information.

538 ## Author Contributions

539 K.T. and W.A.B. participated in the conception, experimental design, and interpretation of the data
540 for this work. K.T. was responsible for the acquisition and analysis of data, statistical analysis, and the
541 drafting of the manuscript. R.S. and W.A.B. reviewed and edited the manuscript. All authors reviewed the
542 manuscript, approved its submission, and take full responsibility for the manuscript.

543

544 ## Acknowledgements

545 We express our gratitude to Qin Liu and Eric A. Pierce of Harvard Medical School for providing the
546 RP1 antibody [65]; Penn Vet Imaging Core Facility (Research Resource Identifier: SCR_022764) for
547 technical support; the staff of the Division of Experimental Retinal Therapies for their excellent support;
548 and the staff of RDSF at University of Pennsylvania for their outstanding animal care. This study was
549 supported by NIH grants R01EY006855, R01EY017549, R01EY033049, P30EY001583, S10OD032305-
550 01A1, and Foundation Fighting Blindness.

551

552 ## Conflict of interest

553 The authors declare that the research was conducted in the absence of any commercial or financial
554 relationships that could be construed as a potential conflict of interest.

555

556 **References**

557 1. Lamb TD, Collin SP, Pugh EN, Jr. Evolution of the vertebrate eye: opsins, photoreceptors, retina
558 and eye cup. Nat Rev Neurosci. 2007;8(12):960-76. doi: 10.1038/nrn2283. PMCID: PMC3143066.

559 2. Park K, Leroux MR. Composition, organization and mechanisms of the transition zone, a gate for
560 the cilium. EMBO Rep. 2022;23(12):e55420. Epub 20221121. doi: 10.15252/embr.202255420. PMCID:
561 PMC9724682.

562 3. Mercey O, Mukherjee S, Guichard P, Hamel V. The molecular architecture of the ciliary transition
563 zones. Curr Opin Cell Biol. 2024;88:102361. Epub 20240421. doi: 10.1016/j.ceb.2024.102361.

564 4. Barnes CL, Malhotra H, Calvert PD. Compartmentalization of Photoreceptor Sensory Cilia. Front
565 Cell Dev Biol. 2021;9:636737. Epub 20210204. doi: 10.3389/fcell.2021.636737. PMCID: PMC7889997.

566 5. Gilliam JC, Chang JT, Sandoval IM, Zhang Y, Li T, Pittler SJ, et al. Three-dimensional architecture
567 of the rod sensory cilium and its disruption in retinal neurodegeneration. Cell. 2012;151(5):1029-41. doi:
568 10.1016/j.cell.2012.10.038. PMCID: PMC3582337.

569 6. Rachel RA, Yamamoto EA, Dewanjee MK, May-Simera HL, Sergeev YV, Hackett AN, et al.
570 CEP290 alleles in mice disrupt tissue-specific cilia biogenesis and recapitulate features of syndromic
571 ciliopathies. Hum Mol Genet. 2015;24(13):3775-91. Epub 20150409. doi: 10.1093/hmg/ddv123. PMCID:
572 PMC4459394.

573 7. Pulvermüller A, Giessl A, Heck M, Wottrich R, Schmitt A, Ernst OP, et al. Calcium-dependent
574 assembly of centrin-G-protein complex in photoreceptor cells. Mol Cell Biol. 2002;22(7):2194-203. doi:
575 10.1128/mcb.22.7.2194-2203.2002. PMCID: PMC133667.

576 8. Sedmak T, Wolfrum U. Intraflagellar transport molecules in ciliary and nonciliary cells of the retina.
577 J Cell Biol. 2010;189(1):171-86. doi: 10.1083/jcb.200911095. PMCID: PMC2854383.

578 9. Sánchez-Bellver L, Toulis V, Marfany G. On the Wrong Track: Alterations of Ciliary Transport in
579 Inherited Retinal Dystrophies. Front Cell Dev Biol. 2021;9:623734. Epub 20210305. doi:
580 10.3389/fcell.2021.623734. PMCID: PMC7973215.

581 10. Wensel TG, Potter VL, Moye A, Zhang Z, Robichaux MA. Structure and dynamics of

582 photoreceptor sensory cilia. Pflugers Arch. 2021;473(9):1517-37. Epub 20210528. doi: 10.1007/s00424-
583 021-02564-9.
584 11. Potter VL, Moye AR, Robichaux MA, Wensel TG. Super-resolution microscopy reveals
585 photoreceptor-specific subciliary location and function of ciliopathy-associated protein CEP290. JCI
586 Insight. 2021;6(20). Epub 20211022. doi: 10.1172/jci.insight.145256. PMCID: PMC8564900.
587 12. Haggerty KN, Eshelman SC, Sexton LA, Frimpong E, Rogers LM, Agosto MA, et al. Super-
588 resolution mapping in rod photoreceptors identifies rhodopsin trafficking through the inner segment
589 plasma membrane as an essential subcellular pathway. PLoS Biol. 2024;22(1):e3002467. Epub
590 20240108. doi: 10.1371/journal.pbio.3002467. PMCID: PMC10773939.
591 13. Robichaux MA, Potter VL, Zhang Z, He F, Liu J, Schmid MF, et al. Defining the layers of a sensory
592 cilium with STORM and cryoelectron nanoscopy. Proc Natl Acad Sci U S A. 2019;116(47):23562-72. Epub
593 20191105. doi: 10.1073/pnas.1902003116. PMCID: PMC6876244.
594 14. Chen F, Tillberg PW, Boyden ES. Optical imaging. Expansion microscopy. Science.
595 2015;347(6221):543-8. Epub 20150115. doi: 10.1126/science.1260088. PMCID: PMC4312537.
596 15. Hümpfer N, Thielhorn R, Ewers H. Expanding boundaries - a cell biologist's guide to expansion
597 microscopy. J Cell Sci. 2024;137(7). Epub 20240417. doi: 10.1242/jcs.260765. PMCID: PMC11058692.
598 16. Moye AR, Robichaux MA, Wensel T. Expansion Microscopy of Mouse Photoreceptor Cilia. Adv
599 Exp Med Biol. 2023;1415:395-402. doi: 10.1007/978-3-031-27681-1_58. PMCID: PMC10697808.
600 17. Verschueren A, Boucherit L, Ferrari U, Fouquet S, Nouvel-Jaillard C, Paques M, et al. Planar
601 polarity in primate cone photoreceptors: a potential role in Stiles Crawford effect phototropism. Commun
602 Biol. 2022;5(1):89. Epub 20220124. doi: 10.1038/s42003-021-02998-y. PMCID: PMC8786850.
603 18. Mercey O, Kostic C, Bertiaux E, Giroud A, Sadian Y, Gaboriau DCA, et al. The connecting cilium
604 inner scaffold provides a structural foundation that protects against retinal degeneration. PLoS Biol.
605 2022;20(6):e3001649. Epub 20220616. doi: 10.1371/journal.pbio.3001649. PMCID: PMC9202906.
606 19. Gambarotto D, Zwettler FU, Le Guennec M, Schmidt-Cernohorska M, Fortun D, Borgers S, et al.
607 Imaging cellular ultrastructures using expansion microscopy (U-ExM). Nat Methods. 2019;16(1):71-4.

608 Epub 20181217. doi: 10.1038/s41592-018-0238-1. PMCID: PMC6314451.
609 20. Arsenijevic Y, Chang N, Mercey O, El Fersioui Y, Koskiniemi-Kuendig H, Joubert C, et al. Fine-
610 tuning FAM161A gene augmentation therapy to restore retinal function. EMBO Mol Med. 2024;16(4):805-
611 22. Epub 20240319. doi: 10.1038/s44321-024-00053-x. PMCID: PMC11018783.
612 21. Faber S, Mercey O, Junger K, Garanto A, May-Simera H, Ueffing M, et al. Gene augmentation of
613 LCA5-associated Leber congenital amaurosis ameliorates bulge region defects of the photoreceptor
614 ciliary axoneme. JCI Insight. 2023;8(10). Epub 20230522. doi: 10.1172/jci.insight.169162. PMCID:
615 PMC10322687.
616 22. Slijkerman RW, Song F, Astuti GD, Huynen MA, van Wijk E, Stieger K, et al. The pros and cons
617 of vertebrate animal models for functional and therapeutic research on inherited retinal dystrophies. Prog
618 Retin Eye Res. 2015;48:137-59. Epub 20150501. doi: 10.1016/j.preteyeres.2015.04.004.
619 23. Kostic C, Arsenijevic Y. Animal modelling for inherited central vision loss. J Pathol.
620 2016;238(2):300-10. Epub 20151113. doi: 10.1002/path.4641. PMC5063185.
621 24. Sahly I, Dufour E, Schietroma C, Michel V, Bahloul A, Perfettini I, et al. Localization of Usher 1
622 proteins to the photoreceptor calyceal processes, which are absent from mice. J Cell Biol.
623 2012;199(2):381-99. Epub 20121008. doi: 10.1083/jcb.201202012. PMCID: PMC3471240.
624 25. Beltran WA, Cideciyan AV, Guziewicz KE, Iwabe S, Swider M, Scott EM, et al. Canine retina has
625 a primate fovea-like bouquet of cone photoreceptors which is affected by inherited macular degenerations.
626 PLoS One. 2014;9(3):e90390. Epub 20140305. doi: 10.1371/journal.pone.0090390. PMCID:
627 PMC3944008.
628 26. Winkler PA, Occelli LM, Petersen-Jones SM. Large Animal Models of Inherited Retinal
629 Degenerations: A Review. Cells. 2020;9(4). Epub 20200403. doi: 10.3390/cells9040882. PMCID:
630 PMC7226744.
631 27. Uzbekov RE, Maurel DB, Aveline PC, Pallu S, Benhamou CL, Rochefort GY. Centrosome fine
632 ultrastructure of the osteocyte mechanosensitive primary cilium. Microsc Microanal. 2012;18(6):1430-41.
633 Epub 20121121. doi: 10.1017/s1431927612013281.

634 28. Langner E, Puapatanakul P, Pudlowski R, Alsabbagh DY, Miner JH, Horani A, et al. Ultrastructure
635 expansion microscopy (U-ExM) of mouse and human kidneys for analysis of subcellular structures.
636 Cytoskeleton (Hoboken). 2024. Epub 20240507. doi: 10.1002/cm.21870.
637 29. Dekomien G, Vollrath C, Petrasch-Parwez E, Boevé MH, Akkad DA, Gerding WM, et al.
638 Progressive retinal atrophy in Schapendoes dogs: mutation of the newly identified CCDC66 gene.
639 Neurogenetics. 2010;11(2):163-74. Epub 20090924. doi: 10.1007/s10048-009-0223-z.
640 30. Gerding WM, Schreiber S, Schulte-Middelmann T, de Castro Marques A, Atorf J, Akkad DA, et al.
641 Ccdc66 null mutation causes retinal degeneration and dysfunction. Hum Mol Genet. 2011;20(18):3620-
642 31. Epub 20110616. doi: 10.1093/hmg/ddr282.
643 31. Murgiano L, Becker D, Spector C, Carlin K, Santana E, Niggel JK, et al. CCDC66 frameshift
644 variant associated with a new form of early-onset progressive retinal atrophy in Portuguese Water Dogs.
645 Sci Rep. 2020;10(1):21162. Epub 20201203. doi: 10.1038/s41598-020-77980-5. PMCID: PMC7712861.
646 32. Odabasi E, Conkar D, Deretic J, Batman U, Frikstad KM, Patzke S, et al. CCDC66 regulates
647 primary cilium length and signaling via interactions with transition zone and axonemal proteins. J Cell Sci.
648 2023;136(3). Epub 20230202. doi: 10.1242/jcs.260327.
649 33. Forman OP, Hitti RJ, Boursnell M, Miyadera K, Sargan D, Mellersh C. Canine genome assembly
650 correction facilitates identification of a MAP9 deletion as a potential age of onset modifier for RPGRIP1-
651 associated canine retinal degeneration. Mamm Genome. 2016;27(5-6):237-45. Epub 20160326. doi:
652 10.1007/s00335-016-9627-x.
653 34. Takahashi K, Kwok JC, Sato Y, Aguirre GD, Miyadera K. Molecular characterization of MAP9 in
654 the photoreceptor sensory cilia as a modifier in canine RPGRIP1-associated cone-rod dystrophy. Front
655 Cell Neurosci. 2023;17:1226603. Epub 20230815. doi: 10.3389/fncel.2023.1226603. PMCID:
656 PMC10464610.
657 35. Ishikawa H, Marshall WF. Intraflagellar Transport and Ciliary Dynamics. Cold Spring Harb
658 Perspect Biol. 2017;9(3). Epub 20170301. doi: 10.1101/cshperspect.a021998. PMCID: PMC5334256.
659 36. Bhogaraju S, Engel BD, Lorentzen E. Intraflagellar transport complex structure and cargo

660 interactions. Cilia. 2013;2(1):10. Epub 20130814. doi: 10.1186/2046-2530-2-10. PMCID: PMC3751104.
661 37. Yang TT, Chong WM, Wang WJ, Mazo G, Tanos B, Chen Z, et al. Super-resolution architecture
662 of mammalian centriole distal appendages reveals distinct blade and matrix functional components. Nat
663 Commun. 2018;9(1):2023. Epub 20180522. doi: 10.1038/s41467-018-04469-1. PMCID: PMC5964178.
664 38. Hazime KS, Zhou Z, Joachimiak E, Bulgakova NA, Wloga D, Malicki JJ. STORM imaging reveals
665 the spatial arrangement of transition zone components and IFT particles at the ciliary base in
666 Tetrahymena. Sci Rep. 2021;11(1):7899. Epub 20210412. doi: 10.1038/s41598-021-86909-5. PMCID:
667 PMC8041816.
668 39. Graser S, Stierhof YD, Lavoie SB, Gassner OS, Lamla S, Le Clech M, et al. Cep164, a novel
669 centriole appendage protein required for primary cilium formation. J Cell Biol. 2007;179(2):321-30. doi:
670 10.1083/jcb.200707181. PMCID: PMC2064767.
671 40. Katoh Y, Chiba S, Nakayama K. Practical method for superresolution imaging of primary cilia and
672 centrioles by expansion microscopy using an amplibody for fluorescence signal amplification. Mol Biol
673 Cell. 2020;31(20):2195-206. Epub 20200729. doi: 10.1091/mbc.E20-04-0250. PMCID: PMC7550703.
674 41. Bowler M, Kong D, Sun S, Nanjundappa R, Evans L, Farmer V, et al. High-resolution
675 characterization of centriole distal appendage morphology and dynamics by correlative STORM and
676 electron microscopy. Nat Commun. 2019;10(1):993. Epub 20190301. doi: 10.1038/s41467-018-08216-4.
677 PMCID: PMC6397210.
678 42. Otto EA, Hurd TW, Airik R, Chaki M, Zhou W, Stoetzel C, et al. Candidate exome capture identifies
679 mutation of SDCCAG8 as the cause of a retinal-renal ciliopathy. Nat Genet. 2010;42(10):840-50. Epub
680 20100912. doi: 10.1038/ng.662. PMCID: PMC2947620.
681 43. Tsutsumi R, Chaya T, Tsujii T, Furukawa T. The carboxyl-terminal region of SDCCAG8 comprises
682 a functional module essential for cilia formation as well as organ development and homeostasis. J Biol
683 Chem. 2022;298(3):101686. Epub 20220204. doi: 10.1016/j.jbc.2022.101686. PMCID: PMC8902618.
684 44. Chong WM, Wang WJ, Lo CH, Chiu TY, Chang TJ, Liu YP, et al. Super-resolution microscopy
685 reveals coupling between mammalian centriole subdistal appendages and distal appendages. Elife.

686 2020;9. Epub 20200403. doi: 10.7554/eLife.53580. PMCID: PMC7173962.
687 45. Yang J, Liu X, Yue G, Adamian M, Bulgakov O, Li T. Rootletin, a novel coiled-coil protein, is a
688 structural component of the ciliary rootlet. J Cell Biol. 2002;159(3):431-40. Epub 20021111. doi:
689 10.1083/jcb.200207153. PMCID: PMC2173070.
690 46. Ryu S, Ko D, Shin B, Rhee K. The intercentriolar fibers function as docking sites of centriolar
691 satellites for cilia assembly. J Cell Biol. 2024;223(4). Epub 20240228. doi: 10.1083/jcb.202105065.
692 PMCID: PMC10901237.
693 47. Yang J, Gao J, Adamian M, Wen XH, Pawlyk B, Zhang L, et al. The ciliary rootlet maintains long-
694 term stability of sensory cilia. Mol Cell Biol. 2005;25(10):4129-37. doi: 10.1128/mcb.25.10.4129-
695 4137.2005. PMCID: PMC1087714.
696 48. Hua K, Ferland RJ. Fixation methods can differentially affect ciliary protein immunolabeling. Cilia.
697 2017;6:5. Epub 20170324. doi: 10.1186/s13630-017-0045-9. PMCID: PMC5366141.
698 49. Gigante ED, Taylor MR, Ivanova AA, Kahn RA, Caspary T. ARL13B regulates Sonic hedgehog
699 signaling from outside primary cilia. Elife. 2020;9. Epub 20200304. doi: 10.7554/eLife.50434. PMCID:
700 PMC7075693.
701 50. Cantagrel V, Silhavy JL, Bielas SL, Swistun D, Marsh SE, Bertrand JY, et al. Mutations in the cilia
702 gene ARL13B lead to the classical form of Joubert syndrome. Am J Hum Genet. 2008;83(2):170-9. doi:
703 10.1016/j.ajhg.2008.06.023. PMCID: PMC2495072.
704 51. Kim YK, Kim JH, Yu YS, Ko HW, Kim JH. Localization of primary cilia in mouse retina. Acta
705 Histochem. 2013;115(8):789-94. Epub 20130419. doi: 10.1016/j.acthis.2013.03.005.
706 52. Rashidi H, Leong YC, Venner K, Pramod H, Fei QZ, Jones OJR, et al. Generation of 3D retinal
707 tissue from human pluripotent stem cells using a directed small molecule-based serum-free microwell
708 platform. Sci Rep. 2022;12(1):6646. Epub 20220422. doi: 10.1038/s41598-022-10540-1. PMCID:
709 PMC9033780.
710 53. Travis AM, Manocha S, Willer JR, Wessler TS, Skiba NP, Pearring JN. Disrupting the ciliary
711 gradient of active Arl3 affects rod photoreceptor nuclear migration. Elife. 2023;12. Epub 20230104. doi:

712 10.7554/eLife.80533. PMCID: PMC9831603.

713 54. Dilan TL, Moye AR, Salido EM, Saravanan T, Kolandaivelu S, Goldberg AFX, et al. ARL13B, a
714 Joubert Syndrome-Associated Protein, Is Critical for Retinogenesis and Elaboration of Mouse
715 Photoreceptor Outer Segments. J Neurosci. 2019;39(8):1347-64. Epub 20181220. doi:
716 10.1523/jneurosci.1761-18.2018. PMCID: PMC6381253.

717 55. Hanke-Gogokhia C, Wu Z, Sharif A, Yazigi H, Frederick JM, Baehr W. The guanine nucleotide
718 exchange factor Arf-like protein 13b is essential for assembly of the mouse photoreceptor transition zone
719 and outer segment. J Biol Chem. 2017;292(52):21442-56. Epub 20171031. doi:
720 10.1074/jbc.RA117.000141. PMCID: PMC5766971.

721 56. Mustafi D, Engel AH, Palczewski K. Structure of cone photoreceptors. Prog Retin Eye Res.
722 2009;28(4):289-302. Epub 20090606. doi: 10.1016/j.preteyeres.2009.05.003. PMCID: PMC2740621.

723 57. Wiik AC, Wade C, Biagi T, Ropstad EO, Bjerkås E, Lindblad-Toh K, et al. A deletion in
724 nephronophthisis 4 (NPHP4) is associated with recessive cone-rod dystrophy in standard wire-haired
725 dachshund. Genome Res. 2008;18(9):1415-21. Epub 20080807. doi: 10.1101/gr.074302.107. PMCID:
726 PMC2527698.

727 58. Goldstein O, Mezey JG, Schweitzer PA, Boyko AR, Gao C, Bustamante CD, et al. IQCB1 and
728 PDE6B mutations cause similar early onset retinal degenerations in two closely related terrier dog breeds.
729 Invest Ophthalmol Vis Sci. 2013;54(10):7005-19. Epub 20131025. doi: 10.1167/iovs.13-12915. PMCID:
730 PMC3809947.

731 59. Mellersh CS, Boursnell ME, Pettitt L, Ryder EJ, Holmes NG, Grafham D, et al. Canine RPGRIP1
732 mutation establishes cone-rod dystrophy in miniature longhaired dachshunds as a homologue of human
733 Leber congenital amaurosis. Genomics. 2006;88(3):293-301. Epub 20060627. doi:
734 10.1016/j.ygeno.2006.05.004.

735 60. Patil H, Tserentsoodol N, Saha A, Hao Y, Webb M, Ferreira PA. Selective loss of RPGRIP1-
736 dependent ciliary targeting of NPHP4, RPGR and SDCCAG8 underlies the degeneration of photoreceptor
737 neurons. Cell Death Dis. 2012;3(7):e355. Epub 20120719. doi: 10.1038/cddis.2012.96. PMCID:

738 PMC3406595.
739 61. Ripolles-Garcia A, Murgiano L, Ziolkowska N, Marinho FP, Roszak K, Iffrig S, et al. Natural
740 disease history of a canine model of oligogenic RPGRIP1-cone-rod dystrophy establishes variable effects
741 of previously and newly mapped modifier loci. Hum Mol Genet. 2023;32(13):2139-51. doi:
742 10.1093/hmg/ddad046. PMCID: PMC10281748.
743 62. Zhang Q, Acland GM, Wu WX, Johnson JL, Pearce-Kelling S, Tulloch B, et al. Different RPGR
744 exon ORF15 mutations in Canids provide insights into photoreceptor cell degeneration. Hum Mol Genet.
745 2002;11(9):993-1003. doi: 10.1093/hmg/11.9.993.
746 63. Aguirre GD, Cideciyan AV, Dufour VL, Ripolles-García A, Sudharsan R, Swider M, et al. Gene
747 therapy reforms photoreceptor structure and restores vision in NPHP5-associated Leber congenital
748 amaurosis. Mol Ther. 2021;29(8):2456-68. Epub 20210327. doi: 10.1016/j.ymthe.2021.03.021. PMCID:
749 PMC8353203.
750 64. Beltran WA, Cideciyan AV, Iwabe S, Swider M, Kosyk MS, McDaid K, et al. Successful arrest of
751 photoreceptor and vision loss expands the therapeutic window of retinal gene therapy to later stages of
752 disease. Proc Natl Acad Sci U S A. 2015;112(43):E5844-53. Epub 20151012. doi:
753 10.1073/pnas.1509914112. PMCID: PMC4629324.
754 65. Liu Q, Zhou J, Daiger SP, Farber DB, Heckenlively JR, Smith JE, et al. Identification and
755 subcellular localization of the RP1 protein in human and mouse photoreceptors. Invest Ophthalmol Vis
756 Sci. 2002;43(1):22-32. PMCID: PMC1963488.
757

758 ## Figure legends

759 **Figure 1. Schematic diagram of the rod photoreceptor sensory cilium**

760 Overall view of the architecture of the rod photoreceptor (left) and detailed depiction of each compartment
761 in the PSC (right). The PSC tubulin axoneme originates from the BB, specifically the MC, located in the
762 IS and extends through the CC to reach the OS. Just beyond the CC, the axoneme expands at the BR
763 and then tapers toward the distal part of the OS. Abbreviations: BB, basal body; BR, bulge region; CC,
764 connecting cilium; DA, distal axoneme; DC, daughter centriole; IS, inner segment; MC, mother centriole;
765 ONL, outer nuclear layer; OS, outer segment; PSC, photoreceptor sensory cilium.

766

767 **Figure 2. Comparison of tissue integrity and protein localization under different U-ExM conditions**

768 **(A-D)** Low-magnification images of the outer retina stained for rhodopsin (yellow), cone arrestin (CAR;
769 cyan), and α-tubulin (magenta) in U-ExM samples subjected to different preservation/fixation protocols
770 (fresh/short-fix, A; fresh/long-fix, B; frozen/long-fix, C) and non-expanded samples (D). Scale bars: 5 μm,
771 without correction for expansion factor. **(E)** Widefield view of a U-ExM sample stained for α-tubulin
772 (yellow) and acetylated α-tubulin (AcTub; magenta). Scale bar: 5 μm, without correction for expansion
773 factor. **(F-I)** Details of α-tubulin (yellow) and AcTub (magenta) staining in the canine PSC under U-ExM
774 (F-H) and non-expanded (I) conditions. The lower panels show axial view at the CC for each U-ExM
775 condition, indicated by white arrowheads. Scale bars: lateral view = 1 μm; axial view = 200 nm, without
776 correction for expansion factor. **(J, K)** Widths of AcTub-labeled CC (J) and MC proximal end (K) under
777 different U-ExM conditions. Sample size: n = 40 photoreceptors. For each condition, 4 individual punches
778 or cryosections from 2-4 eyes were stained. Non-significant (n.s., $P > 0.05$) as assessed by Kruskal-
779 Wallis test with Dunn's multiple-comparison test. **(L-S)** Molecular localization of Centrin (cyan, L-O) and
780 CEP290 (green, P-S) in normal canine PSC under U-ExM with different preservation/fixation protocols
781 (fresh/short-fix, L, P; fresh/long-fix, M, Q; frozen/long-fix, N, R) and non-expanded (O, S) conditions.
782 Scale bars: lateral view = 1 μm; axial view = 200 nm, without correction for expansion factor.
783 Abbreviations: CC, connecting cilium; DC, daughter centriole; INL, inner nuclear layer; IS, inner segment;

784 MC, mother centriole; ONL, outer nuclear layer; OS, outer segment; PFA, paraformaldehyde; PSC,
785 photoreceptor sensory cilium.
786
787 **Figure 3. Tubulin-based molecular structure of rod and cone PSC in normal adult canine**
788 **photoreceptors**
789 **(A-D)** Confocal images of expanded adult canine PSC stained for AcTub (magenta) and glutamylated
790 microtubules (white). Rod and cone photoreceptors were identified by labeling with rhodopsin (yellow, A)
791 and cone arrestin (CAR; cyan, C), respectively. Black, red, and white arrowheads on BR, CC, and MC
792 correspond to the respective axial views in (B, D). Scale bars: lateral view = 500 nm; axial view = 200
793 nm, after correction for expansion factor. **(E)** Schematic diagram showing the measurement of length and
794 width in the CC and BB. The tubulin axoneme labeled with AcTub and the glutamylation signals on Y-
795 links are represented in magenta and grey, respectively. **(F-I)** Comparison of length and width on the BB
796 (F, G) and the CC (H, I) between rod and cone PSC. **(J, K)** Rod (J) and cone (K) PSC illustrating the
797 measurements of AcTub-labeled axoneme width at four locations relative to the BR: +1000, +500, 0, and
798 -500 nm. The distal end of the glutamylation signal located outside of the tubulin axoneme was used to
799 define the 0 nm location. Scale bars: 500 nm, after correction for expansion factor. **(L, M)** Measurements
800 of tubulin width in rod (L) and cone (M) PSC at the four locations illustrated in (J, K). **(N)** Comparison of
801 tubulin width between rod and cone photoreceptors at the four locations shown in (J, K). Sample size: n
802 = 12-22 from ≥ 2 individual eyes. *P < 0.05, **P < 0.01, ***P < 0.001, and ****P < 0.0001 as assessed by
803 Kruskal-Wallis test with Dunn's multiple-comparison test (F, G) or Mann–Whitney test (H, I, L-N).
804 Abbreviations: BB, basal body; BR, bulge region; CC, connecting cilium; DC, daughter centriole; MC,
805 mother centriole; PSC, photoreceptor sensory cilium.
806
807 **Figure 4. Molecular architecture of the bulge region and distal axoneme in normal canine rod and**
808 **cone PSC**
809 **(A-F)** Lateral views of expanded adult canine PSC stained for LCA5 (orange, A, B), RP1 (green, C, D),

810 and CCDC66 (white, E, F) in rod (A, C, E) and cone (B, D, F) photoreceptors, respectively. Scale bars:
811 500 nm, after correction for expansion factor. **(G-L)** Co-immunolabeling with LCA5/RP1 (orange/green,
812 G-I) and RP1/CCDC66 (green/white, J-L) in each photoreceptor subtype. The right panels (I, L) show
813 axial views of the BR indicated by the white arrowheads in each staining. The white dashed lines
814 represent the starting position of each protein signal on the tubulin axoneme. Scale bars: lateral view =
815 500 nm; axial view = 200 nm, after correction for expansion factor. **(M)** Comparison of distance from the
816 proximal end of the MC to the starting point of each protein signal between rod and cone PSC. Sample
817 size: n = 12-24 from ≥ 3 individual eyes. ***P < 0.001, and ****P < 0.0001 as assessed by Mann–Whitney
818 test. **(N)** Model illustrating the differences in molecular architecture of the distal part of the PSC, including
819 the BR, between rod and cone photoreceptors. Abbreviations: BR, bulge region; MC, mother centriole;
820 PSC, photoreceptor sensory cilium.
821
822 **Figure 5. Location of inner scaffold proteins in normal canine rod and cone PSC**
823 **(A-I)** Confocal images of expanded adult canine PSC stained for POC5 (green, A-C), Centrin (green, D-
824 F), and FAM161A (green, G-H). Rod and cone photoreceptors were identified by labeling with rhodopsin
825 (yellow, A, D, G) and CAR (cyan, B, E, H), respectively. The right panels (C, F, I) show axial views of the
826 CC for each protein, indicated by white arrowheads. Scale bars: lateral view = 500 nm; axial view = 200
827 nm, after correction for expansion factor. **(J)** Schematic diagram illustrating the measurement of signal
828 length in the CC. The tubulin axoneme labeled with AcTub and inner scaffold proteins are represented in
829 magenta and green, respectively. **(K)** Comparison of POC5 and Centrin signal lengths between rod and
830 cone PSC. Sample size: n = 9-18 from ≥ 2 individual eyes. ****P < 0.0001 as assessed by Mann–Whitney
831 test. Abbreviations: CC, connecting cilium; PSC, photoreceptor sensory cilium.
832
833 **Figure 6. Molecular mapping of multiple connecting cilium-related proteins in normal canine rod**
834 **and cone PSC**
835 **(A-R)** Expanded normal canine PSC stained for CEP290 (green, A-C), RPGR (green, D-F), RPGRIP1

836 (green, G-I), SPATA7 (green, J-L), NPHP5 (green, M-O), and MAP9 (white, P-R) in rod (A, D, G, J, M, P)
837 and cone (B, E, H, K, N, Q) photoreceptors, respectively. Axial views of the CC for each protein, indicated
838 by white arrowheads, are shown in (C, F, I, L, O, R). Scale bars: lateral view = 500 nm; axial view = 200
839 nm, after correction for expansion factor. **(S)** Measurement of signal length of each protein on the CC in
840 rod and cone PSC. Sample size: n = 11-26 from ≥ 3 individual eyes. **(T)** Comparison of signal width
841 between CEP290, MAP9, and AcTub in rod and cone PSC. Sample size: n = 11-35 from ≥ 3 individual
842 eyes. *P < 0.05 and ****P < 0.0001 as assessed by Mann–Whitney test (S) or Kruskal-Wallis test with
843 Dunn's multiple-comparison test (T). Abbreviations: CC, connecting cilium; PSC, photoreceptor sensory
844 cilium.
845
846 **Figure 7. Localization of ciliary trafficking and distal appendage-related proteins in normal canine**
847 **rod and cone PSC**
848 **(A-C)** Confocal U-ExM images of normal canine PSC stained for AcTub (magenta) and IFT57 (green) in
849 rod (A) and cone (B) photoreceptors, respectively. Insets show details of IFT57 location around the MC.
850 Black, red, and white arrowheads on BR, CC, and MC correspond to the axial views shown in (C). Scale
851 bars: lateral view = 500 nm; axial view = 200 nm, after correction for expansion factor. **(D)** Comparison
852 of distance from the proximal end of the MC to IFT57 signals around the basal part of PSC between rod
853 and cone PSC. Sample size: n = 12-20 from ≥ 3 individual eyes. **(E-J)** Expanded normal canine
854 photoreceptors labeled for distal appendage-marker (CEP164; green, E-G) and SDCCAG8 (green, H-J)
855 in rod (E, H) and cone (F, I) photoreceptors, respectively. Axial views of the basal part of PSC for each
856 protein, indicated by white arrowheads, are shown in (G, J). Scale bars: lateral view = 500 nm; axial view
857 = 200 nm, after correction for expansion factor. **(K-L)** Co-immunolabeling with glutamylation/SDCCAG8
858 (white/green, K) and γ-tubulin/SDCCAG8 (orange/green, L). Scale bars: 500 nm, after correction for
859 expansion factor. **(M)** Measurement of distance from the proximal end of the MC to the signal of each
860 protein in rod and cone PSC. Sample size: n = 13-26 from ≥ 3 individual eyes. **P < 0.01, ***P < 0.001,
861 and ****P < 0.0001 as assessed by Mann–Whitney test. **(N)** Model illustrating the identified location of

862 IFT57 and SDCCAG8 around the distal appendages and the BB in normal canine photoreceptors.
863 Abbreviations: BB, basal body; BR, bulge region; CC, connecting cilium; DC, daughter centriole; MC,
864 mother centriole; PSC, photoreceptor sensory cilium.
865
866 **Figure 8. Structural characterization of the ciliary rootlet in normal canine rod and cone**
867 **photoreceptors**
868 **(A)** Widefield view of a U-ExM sample stained for rootletin (green) and AcTub (magenta). Scale bar: 1
869 μm, after correction for expansion factor. **(B-E)** High-magnification of expanded normal canine PSC
870 stained for rootletin (green) and AcTub (magenta) in rod (B, C) and cone (D, E) photoreceptors,
871 respectively. 3D rendering images were shown in (C, E) from different angles. Scale bars: 2D maximum
872 projection = 1 μm; 3D view = 500 nm, after correction for expansion factor. **(F)** Co-immunolabeling with
873 ARL13B/rootletin (white/green) in a U-ExM sample of normal canine retina. Scale bars: 1 μm, after
874 correction for expansion factor. **(G, H)** Confocal images of expanded adult canine photoreceptors stained
875 for ARL13B (white) and AcTub (magenta). Rod and cone photoreceptors were identified by labeling with
876 rhodopsin (yellow, G) and CAR (cyan, H), respectively. Scale bars: low-magnification view = 1 μm; high-
877 magnification view = 500 nm, after correction for expansion factor. Abbreviations: CC, connecting cilium;
878 IS, inner segment; ONL, outer nuclear layer; PSC, photoreceptor sensory cilium.
879
880 **Figure 9. Molecular architecture of calyceal processes in normal canine photoreceptors**
881 **(A)** Widefield view of a non-expanded retinal cryosection stained for rhodopsin (yellow), G protein subunit
882 alpha transducin 1 (GNAT1; orange), and protocadherin 15 (PCDH15; green). The right panels show
883 details of PCDH15 location in rod and cone photoreceptors. Scale bar: 5 μm, without correction for
884 expansion factor. **(B-E)** Confocal images of expanded adult canine photoreceptors stained for PCDH15
885 (green) and AcTub (magenta). Rod and cone photoreceptors were identified by labeling with rhodopsin
886 (yellow, B), CAR (cyan, C), blue-opsin (blue, D), and red/green-opsin (red, E) respectively. The right
887 panels in (B, C) and (E, D) are showing 3D rendering images of one photoreceptor. Scale bars: 500 nm,

888 after correction for expansion factor. **(F)** Co-immunolabeling with PCDH15/β-actin (green/orange) in a U-
889 ExM sample of normal canine retina. The right panels show details of calyceal processes in cone
890 photoreceptor with a 2D maximum projection (upper) and a 3D rendering image (lower). Scale bars: low-
891 magnification view = 1 μm; high-magnification view = 500 nm, after correction for expansion factor. **(G)**
892 Model illustrating the identified location of proteins related to calyceal processes in canine photoreceptors.
893 Abbreviations: IS, inner segment; ONL, outer nuclear layer; OS, outer segment; PSC, photoreceptor
894 sensory cilium.
895
896 **Figure 10. Schematic summary diagrams of the molecular architecture of PSC and calyceal**
897 **processes, and the distribution of retinal ciliopathy-associated proteins in normal canine rod and**
898 **cone photoreceptors**
899 **(A)** Overview of the architecture of normal canine rod (left) and cone (right) photoreceptors. **(B)**
900 Comparison of PSC molecular architecture between rod and cone photoreceptors. Cone PSC has a
901 longer and wider BR, longer BBs, and a shorter CC than those of rod PSC. **(C)** Structural differences of
902 PSC rootlet between rod and cone photoreceptors. Rod photoreceptors have a straight rootlet extending
903 toward the ONL, whereas the rootlet of cones forms a curvilinear shape. **(D)** Distribution of calyceal
904 processes-related proteins in rod and cone photoreceptors. In rod photoreceptors, the localization of
905 PCDH15 is limited to the IS/OS junction, while in cone photoreceptors, PCDH15 shows a microvilli-like
906 distribution accompanied by actin filaments. Abbreviations: BB, basal body; BR, bulge region; CC,
907 connecting cilium; DA, distal axoneme; DC, daughter centriole; IS, inner segment; MC, mother centriole;
908 ONL, outer nuclear layer; OS, outer segment; PSC, photoreceptor sensory cilium.
909
910 **Supplementary Figure 1. Overview of the modified U-ExM protocol for fresh and frozen-archival**
911 **canine retinal tissues**
912 AA, acrylamide; ASP, ammonium persulfate; ddH_2O, distilled deionized water; FA, formaldehyde; MS,
913 monomer solution; OCT, optimal cutting temperature; PFA, paraformaldehyde; RT, room temperature;

914 TEMED, tetramethylethylenediamine.

915

916 **Supplementary Figure 2. Tissue processing and gel expansion in U-ExM with canine retinal**
917 **tissues**

918 **(A)** Collection of 5 mm tissue punches from PFA fixed-fresh canine posterior eyecup using a disposable
919 biopsy punch. **(B, C)** Isolation of retinal tissue from the 5 mm tissue complex (B, before; C, after isolation).
920 **(D)** Gelation of the 5 mm retinal punch using a 12 mm circular cover glass. **(E)** First-round expansion of
921 the gel including the fresh retinal punch. **(F)** Twenty-μm-thick canine retinal cryosection. **(G)** Gelation of
922 the canine retinal cryosection using a 12 mm circular cover glass. **(H)** First-round expansion of the gel
923 including the retinal section. **(I)** Comparison of gel diameter after the first-round expansion between
924 different fixation conditions. Sample size: n = 4 individual punches or cryosections from 2-4 eyes per
925 fixation/storage condition. Non-significant (n.s., $P > 0.05$) by Kruskal-Wallis test with Dunn's multiple-
926 comparison test.

927

928 **Supplementary Figure 3. Co-immunolabeling of CEP290 and glutamination on the connecting**
929 **cilium of normal canine photoreceptors**

930 Confocal images of expanded adult canine PSC stained for AcTub (magenta), glutamination (white), and
931 CEP290 (green). The lower panels show axial views of the CC, indicated by white arrowheads. Scale
932 bars: lateral view = 500 nm; axial view = 200 nm, after correction for expansion factor. Abbreviations: CC,
933 connecting cilium.

934

935 **Supplementary Figure 4. Localization of KIF3A in normal canine rod and cone PSC**

936 **(A, B)** Confocal U-ExM images of normal canine PSC stained for AcTub (magenta) and KIF3A (green) in
937 rod (A) and cone (B) photoreceptors, respectively. KIF3A signal shows a similar localization pattern to
938 IFT57 around the BB and BR. Abbreviations: BB, basal body; BR, bulge region; PSC, photoreceptor
939 sensory cilium.

940

941 **Supplementary Figure 5. Stricture of the PSC rootlet in normal canine blue and red/green cone**
942 **photoreceptors**

943 **(A, B)** 3D rendering images of U-ExM samples stained for rootletin (green) with blue-opsin (blue, A) or
944 red/green-opsin (red, B). No significant differences are observed in the architecture of the PSC rootlet
945 among the different cone subtypes. Scale bars: 500 nm, after correction for expansion factor.
946 Abbreviation: PSC, photoreceptor sensory cilium.

947

948 **Supplementary Figure 6. Immunostaining for ARL13B on non-expanded normal canine retinal**
949 **cryosection**

950 Widefield (left) and high-magnification (right) view of a non-expanded retinal cryosection stained for
951 rhodopsin (yellow), ARL13B (white), and AcTub (magenta). Similar to the U-ExM samples, ARL13B is
952 predominantly localized to the IS in the non-expanded cryosection. Scale bars: 5 μm. Abbreviations: INL,
953 inner nuclear layer; IS, inner segment; ONL, outer nuclear layer; OS, outer segment.

Figure 1

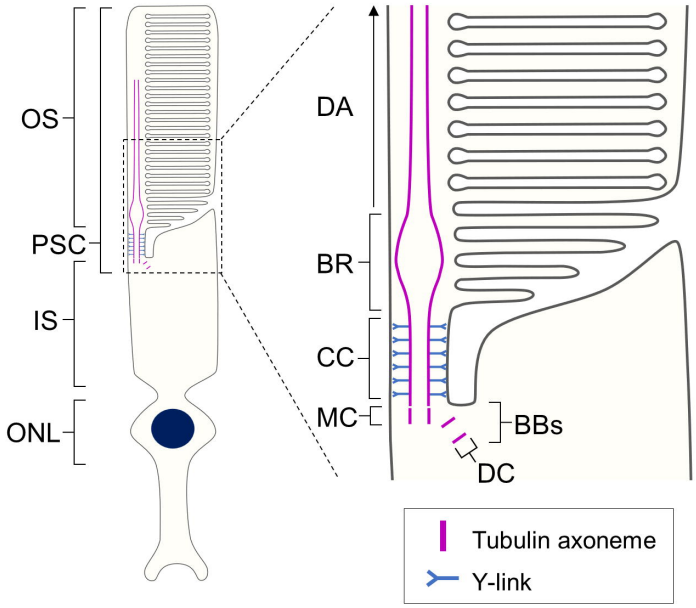

Figure 2

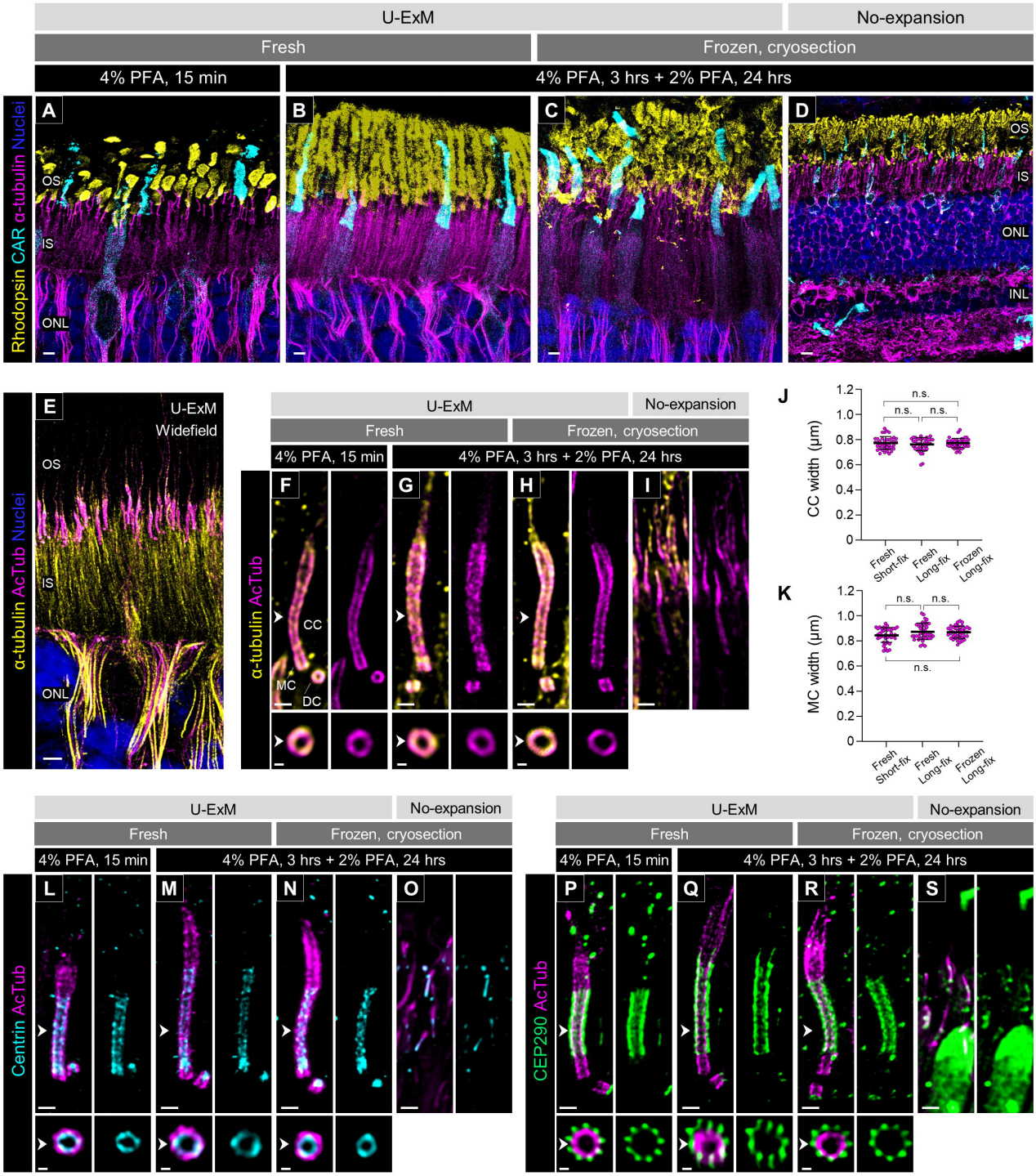
U-ExM
No-expansion
Fresh
Frozen, cryosection
4% PFA, 15 min
4% PFA, 3 hrs + 2% PFA, 24 hrs
Rhodopsin CAR α-tubulin Nuclei
A
B
C
D
OS
IS
ONL
INL
α-tubulin AcTub Nuclei
E
U-ExM
Widefield
α-tubulin AcTub
F
G
H
I
CC
MC
DC
J
CC width (µm)
n.s.
Fresh Short-fix
Fresh Long-fix
Frozen Long-fix
K
MC width (µm)
Centrin AcTub
L
M
N
O
CEP290 AcTub
P
Q
R
S

Figure 3

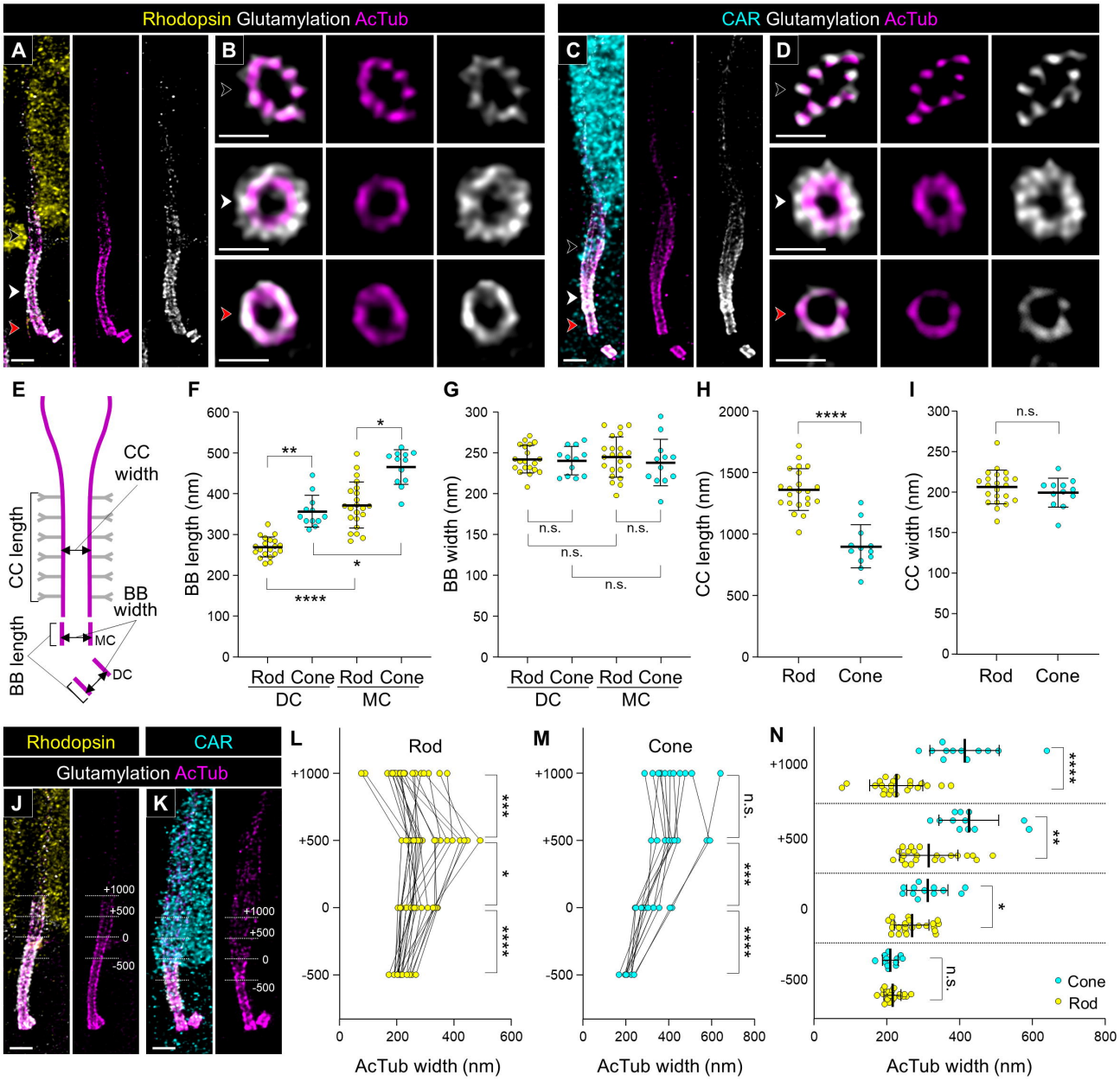
Rhodopsin Glutamylation AcTub
CAR Glutamylation AcTub
A
B
C
D
E
CC width
CC length
BB width
BB length
MC
DC
F
BB length (nm)
Rod Cone Rod Cone
DC MC
G
BB width (nm)
n.s.
H
CC length (nm)
Rod Cone
I
CC width (nm)
Rhodopsin
CAR
Glutamylation AcTub
J
K
L
Rod
M
Cone
N
AcTub width (nm)
Cone
Rod

Figure 4

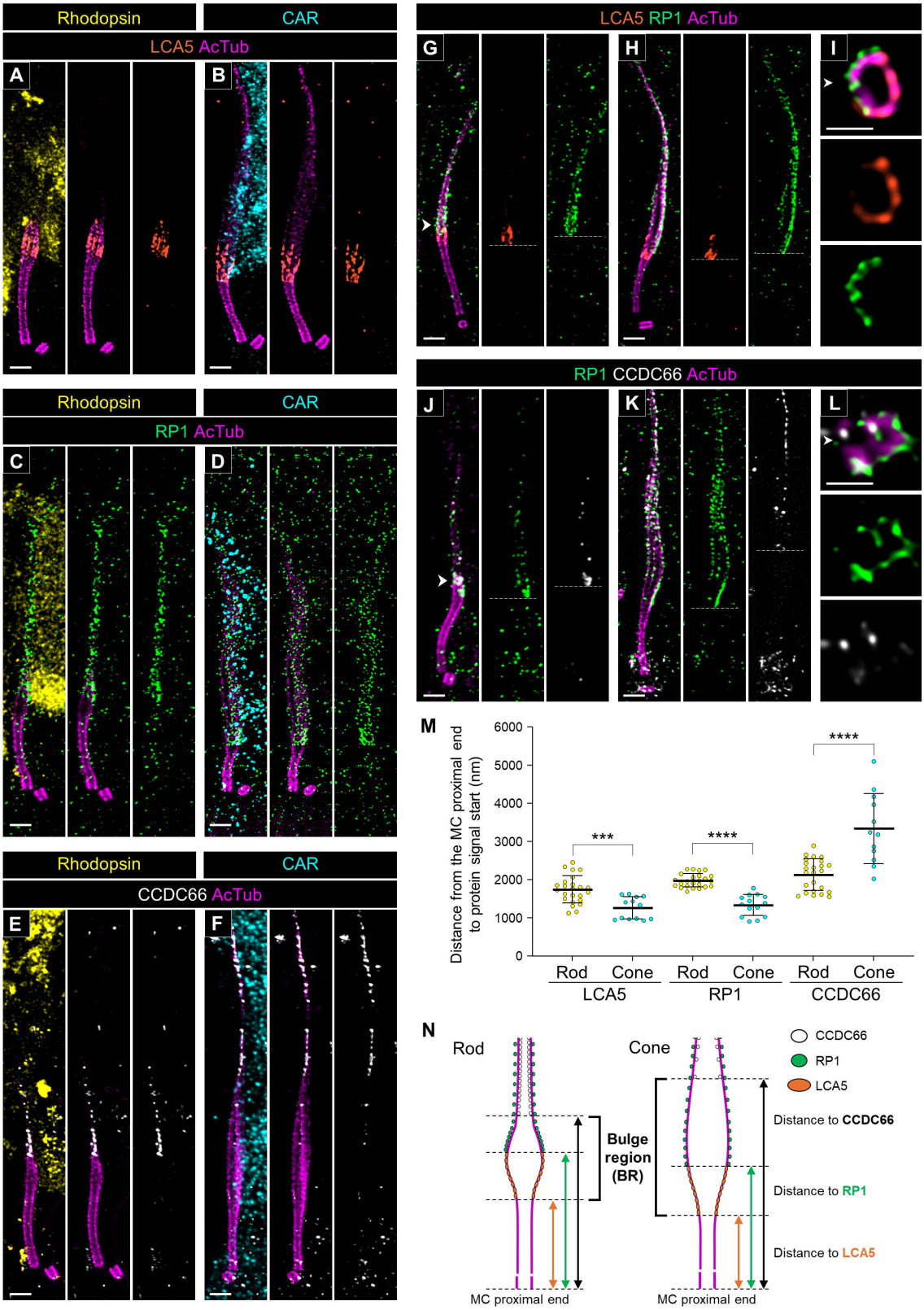
Rhodopsin
CAR
LCA5 AcTub
A
B
Rhodopsin
CAR
RP1 AcTub
C
D
Rhodopsin
CAR
CCDC66 AcTub
E
F
LCA5 RP1 AcTub
G
H
I
RP1 CCDC66 AcTub
J
K
L
M
Distance from the MC proximal end to protein signal start (nm)
6000
5000
4000
3000
2000
1000
0
***
****
****
Rod
Cone
Rod
Cone
Rod
Cone
LCA5
RP1
CCDC66
N
Rod
Cone
CCDC66
RP1
LCA5
Bulge region (BR)
Distance to CCDC66
Distance to RP1
Distance to LCA5
MC proximal end
MC proximal end

Figure 5

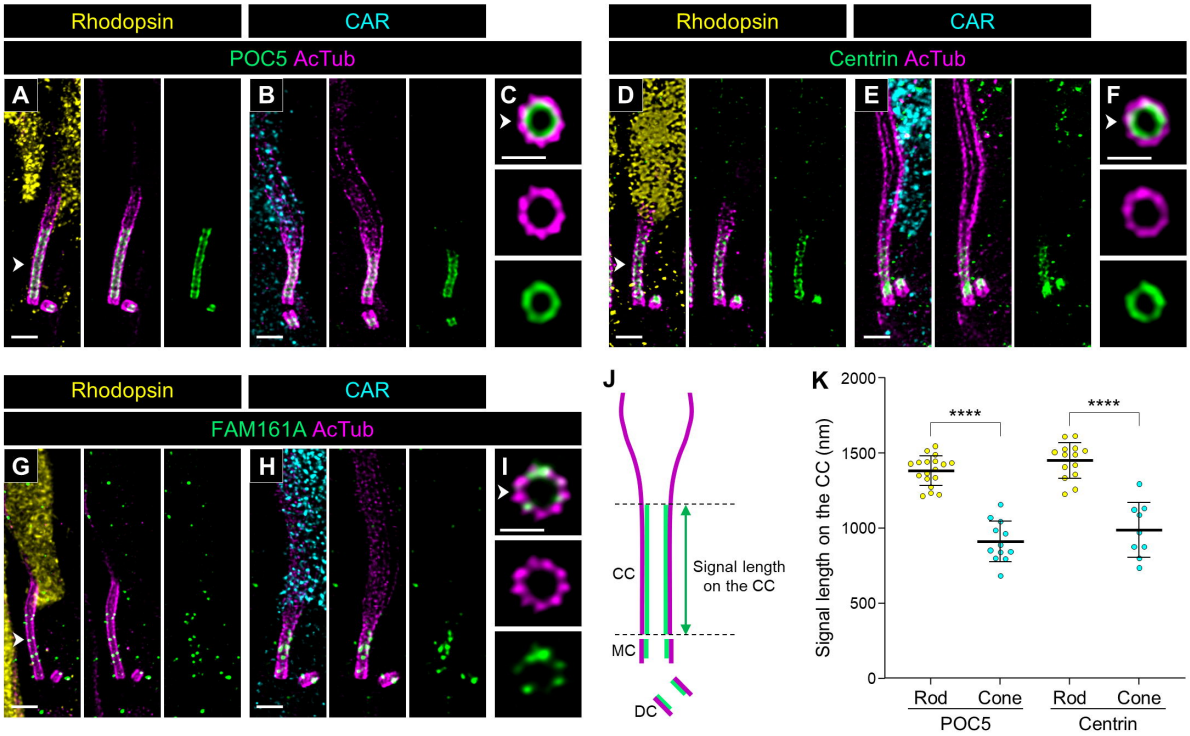
Rhodopsin
CAR
POC5 AcTub
A
B
C
Rhodopsin
CAR
Centrin AcTub
D
E
F
Rhodopsin
CAR
FAM161A AcTub
G
H
I
J
CC
MC
DC
Signal length on the CC
K
Signal length on the CC (nm)
2000
1500
1000
500
0
****
****
Rod
Cone
Rod
Cone
POC5
Centrin

Figure 6

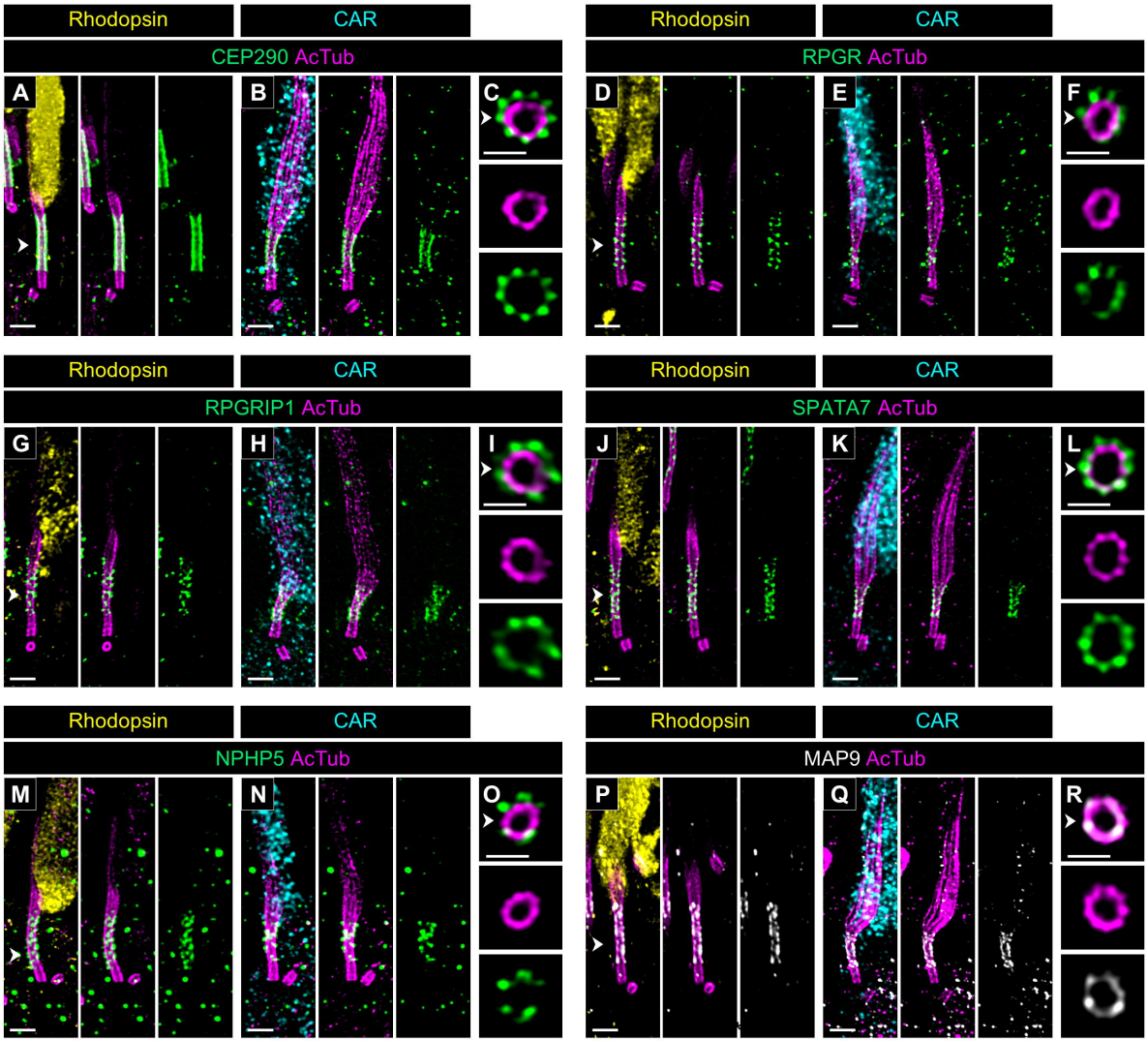
Rhodopsin
CAR
CEP290 AcTub
RPGR AcTub
RPGRIP1 AcTub
SPATA7 AcTub
NPHP5 AcTub
MAP9 AcTub
A
B
C
D
E
F
G
H
I
J
K
L
M
N
O
P
Q
R

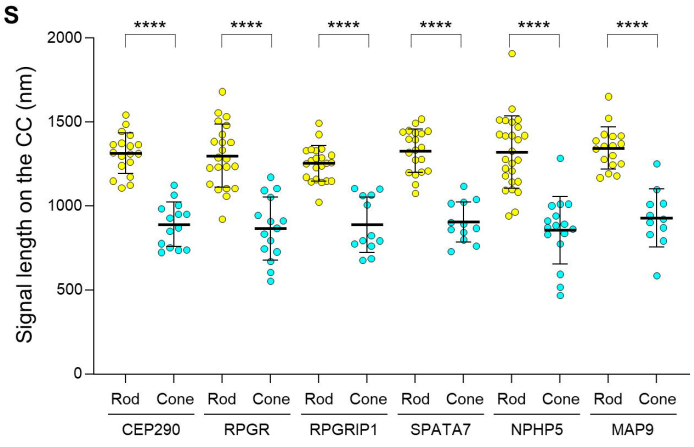
S
Signal length on the CC (nm)
2000
1500
1000
500
0
****
Rod
Cone
CEP290
RPGR
RPGRIP1
SPATA7
NPHP5
MAP9

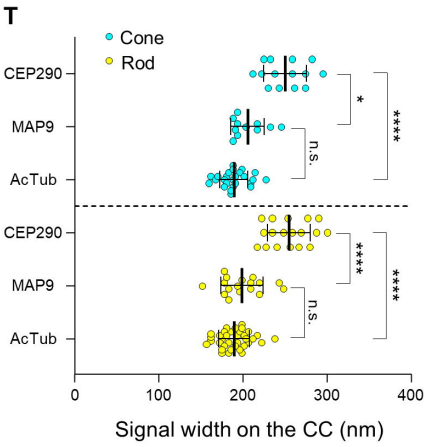
T
Cone
Rod
CEP290
MAP9
AcTub
*
****
n.s.
0
100
200
300
400
Signal width on the CC (nm)

Figure 7

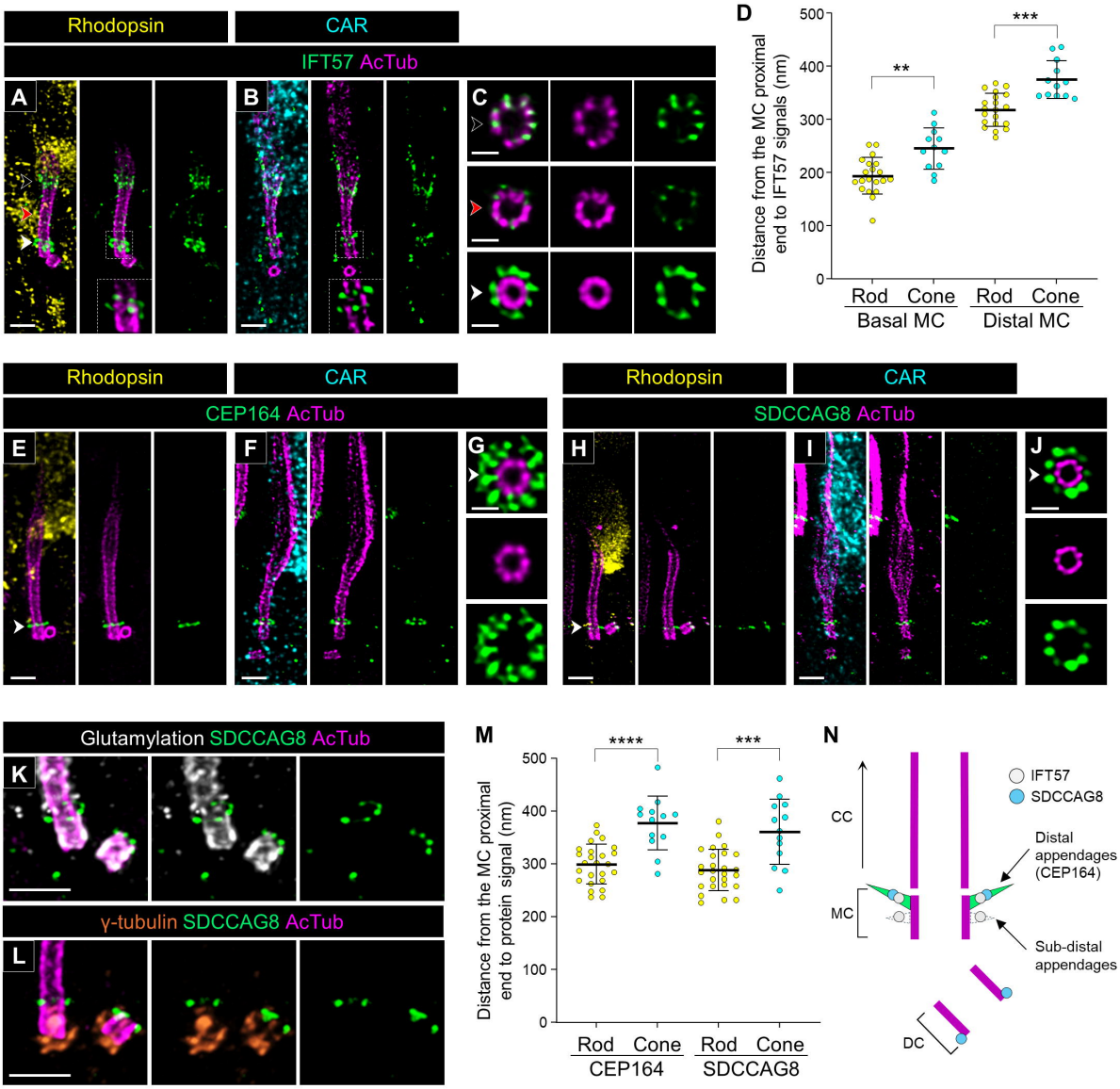
Rhodopsin
CAR
IFT57 AcTub
A
B
C
D
Distance from the MC proximal end to IFT57 signals (nm)
500
400
300
200
100
0
**
***
Rod
Cone
Rod
Cone
Basal MC
Distal MC
Rhodopsin
CAR
CEP164 AcTub
E
F
G
Rhodopsin
CAR
SDCCAG8 AcTub
H
I
J
Glutamylation SDCCAG8 AcTub
K
γ-tubulin SDCCAG8 AcTub
L
M
Distance from the MC proximal end to protein signal (nm)
500
400
300
200
100
0
****
***
Rod
Cone
Rod
Cone
CEP164
SDCCAG8
N
IFT57
SDCCAG8
CC
MC
DC
Distal appendages (CEP164)
Sub-distal appendages

Figure 8

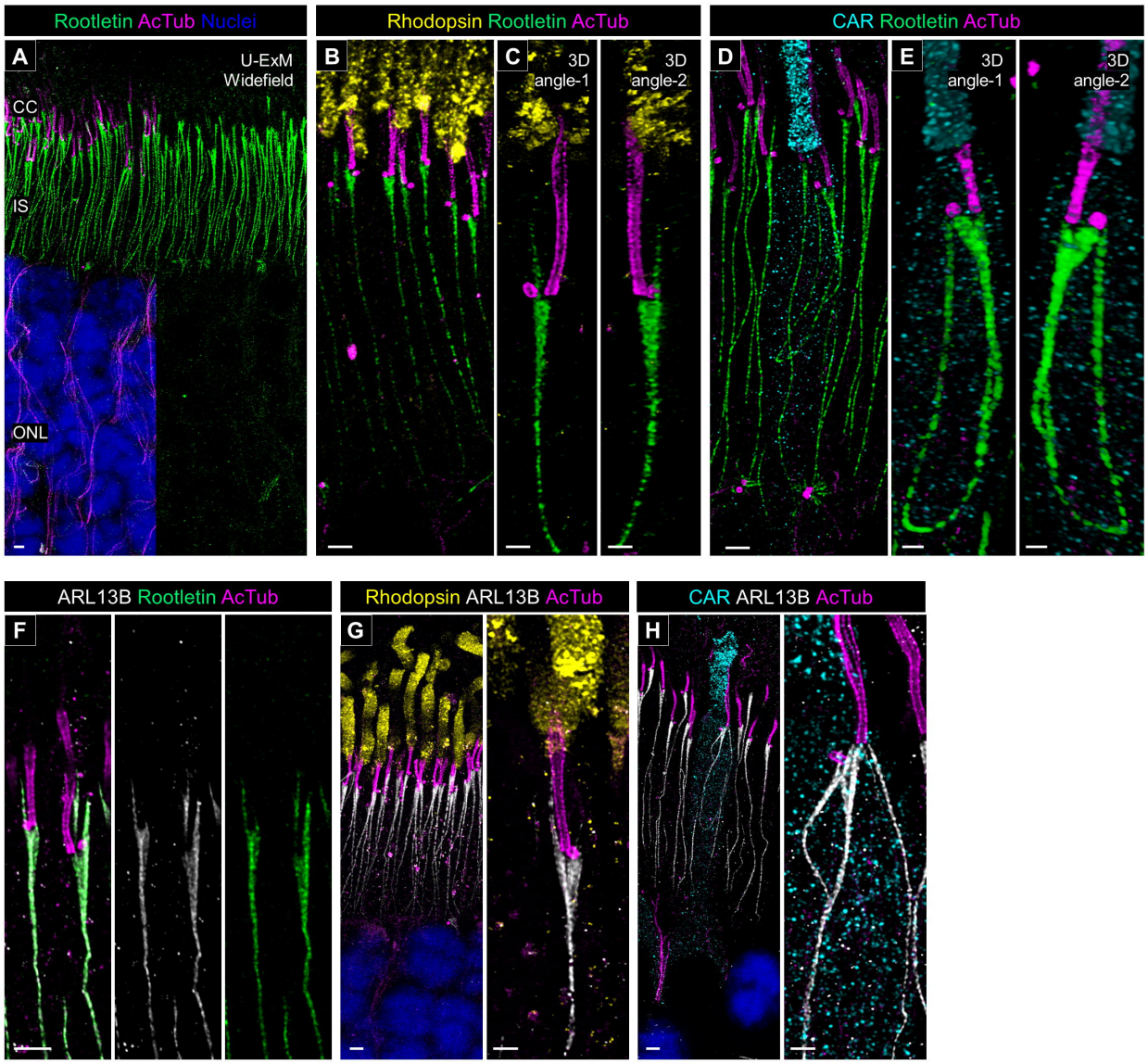
Rootletin AcTub Nuclei
A
U-ExM
Widefield
CC
IS
ONL
Rhodopsin Rootletin AcTub
B
C
3D
angle-1
3D
angle-2
CAR Rootletin AcTub
D
E
3D
angle-1
3D
angle-2
ARL13B Rootletin AcTub
F
Rhodopsin ARL13B AcTub
G
CAR ARL13B AcTub
H

Figure 9

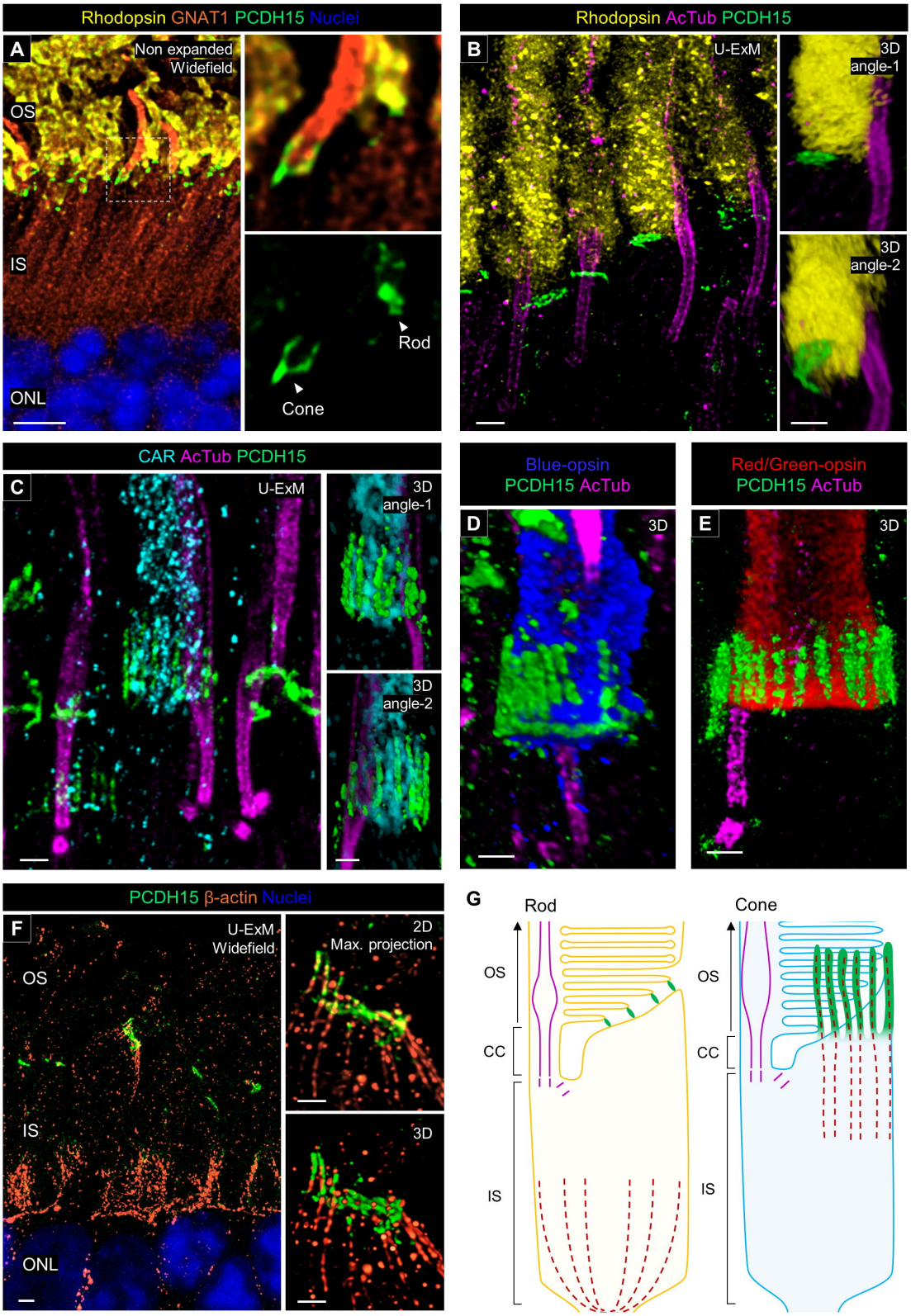
Rhodopsin GNAT1 PCDH15 Nuclei
A
Non expanded
Widefield
OS
IS
ONL
Rod
Cone
Rhodopsin AcTub PCDH15
B
U-ExM
3D
angle-1
3D
angle-2
CAR AcTub PCDH15
C
U-ExM
3D
angle-1
3D
angle-2
Blue-opsin
PCDH15 AcTub
D
3D
Red/Green-opsin
PCDH15 AcTub
E
3D
PCDH15 β-actin Nuclei
F
U-ExM
Widefield
OS
IS
ONL
2D
Max. projection
3D
G
Rod
Cone
OS
CC
IS
OS
CC
IS

Figure 10

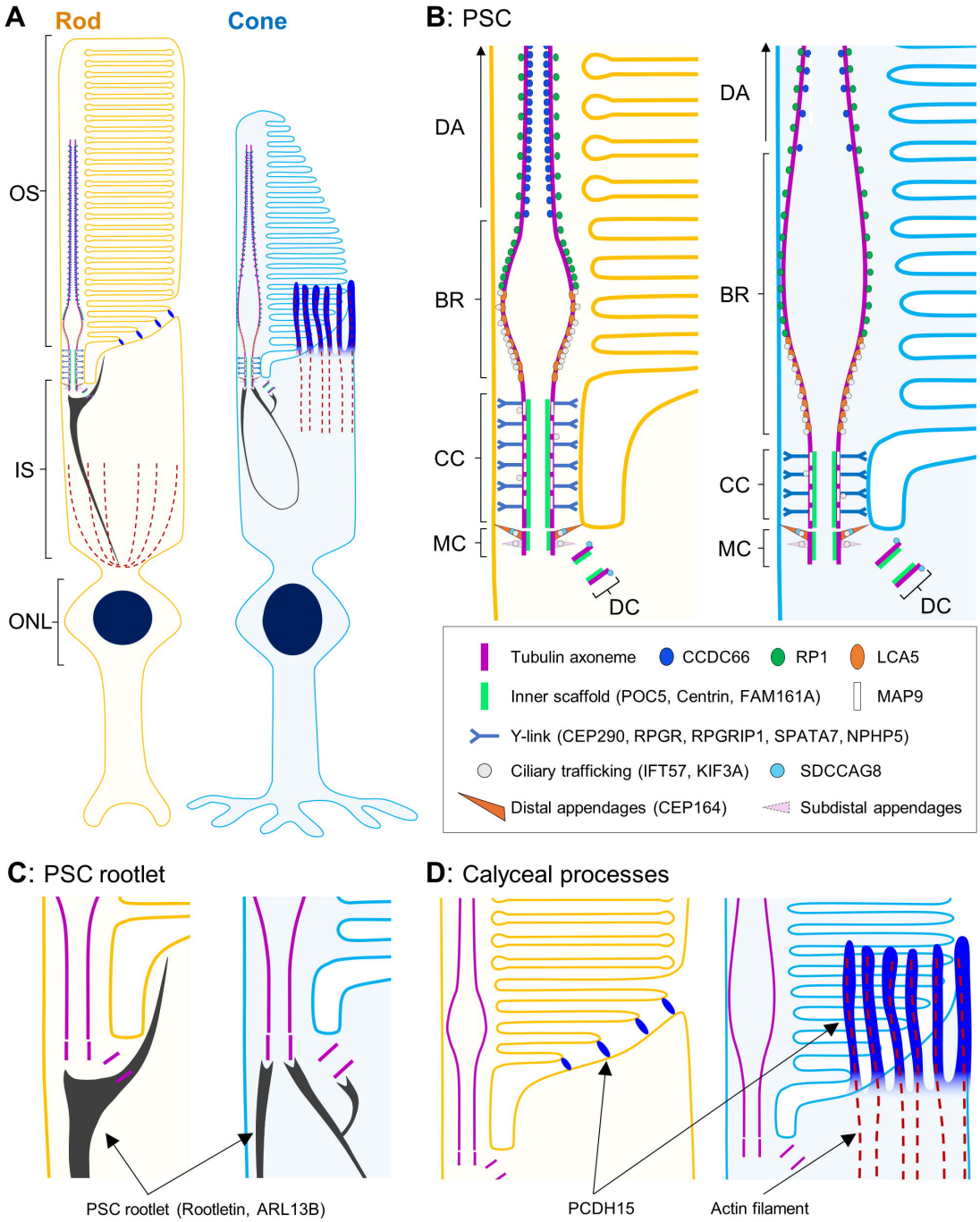
A
Rod
Cone
OS
IS
ONL
B: PSC
DA
BR
CC
MC
DC
Tubulin axoneme
CCDC66
RP1
LCA5
Inner scaffold (POC5, Centrin, FAM161A)
MAP9
Y-link (CEP290, RPGR, RPGRIP1, SPATA7, NPHP5)
Ciliary trafficking (IFT57, KIF3A)
SDCCAG8
Distal appendages (CEP164)
Subdistal appendages
C: PSC rootlet
PSC rootlet (Rootletin, ARL13B)
D: Calyceal processes
PCDH15
Actin filament